Dopaminergic regulation of vestibulo-cerebellar circuits through unipolar brush cells

Jose Ernesto Canton-Josh, Joanna Qin, Yevgenia Kozorovitskiy*

Department of Neurobiology, Northwestern University, Evanston, IL 60208

*Corresponding author: Yevgenia.Kozorovitskiy@northwestern.edu

SUMMARY

While multiple monoamines modulate cerebellar output, the mechanistic details of dopaminergic signaling in the cerebellum remain poorly understood. Here we show that Drd1 dopamine receptors are expressed in unipolar brush cells (UBCs) of the cerebellar vermis. Drd1 activation increases UBC firing rate and postsynaptic NMDA receptor-mediated currents. Purkinje neurons directly inhibit Drd1-positive UBCs, forming a recurrent vestibulo-cerebellar circuit. Using anatomical tracing and *in situ* hybridization, we tested three hypotheses about the source of cerebellar dopamine. We exclude the midbrain dopaminergic nuclei and tyrosine hydroxylase-positive Purkinje cells as potential sources, supporting the possibility of dopaminergic co-release from locus coeruleus (LC) axons. Using an optical dopamine sensor $GRAB_{DA}$, electrical stimulation, and optogenetic activation of LC fibers in the acute slice, we find evidence for monoamine release onto Drd1-expressing UBCs. Altogether, we propose that the LC regulates cerebellar cortex activity by co-releasing dopamine onto UBCs to modulate their response to cerebellar inputs.

INTRODUCTION

Cerebellar activity plays a critical function in fine motor learning (Kalmbach et al., 2010; Raymond and Lisberger, 1998; Woodruff-pak, 1993). The cerebellum is defined by clearly organized cytoarchitecture; however, important anatomical, molecular, and functional differences between lobules are beginning to emerge. These differences include specialized neuronal classes present only in certain regions of the cerebellar cortex. Electrophysiological and behavioral data indicate that these varying motifs are likely relevant for the function of specific lobules in behavior. One key difference between cerebellar lobules is the distribution of unipolar brush cells (UBCs), a glutamatergic interneuron enriched in the granular layer of vestibulo-cerebellum, which is known to be involved in processing vestibular sensory input (Mugnaini and Floris, 1994). UBCs reside in the granular layer and receive inputs from mossy fibers. Each UBC axon diverges, releasing glutamate onto multiple local granule cells or other UBCs. Since UBCs are recurrently connected, they are poised to amplify and temporally extend the influence of excitatory inputs into the cerebellum (Requarth and Sawtell, 2014). Alternatively, UBCs—receiving a single mossy fiber input—could form a 'labeled line' input to the granular layer, helping to distinguish between inputs from semicircular canals and otoliths (Balmer and Trussell, 2019). The relatively recent discovery of UBCs in the late 1970s (Altman and Bayer, 1977) and characterization in the 1990s (Mugnaini and Floris, 1994), their sparseness in the cerebellum, and the lack of tools to isolate them have limited our understanding of their functional connectivity.

Differences in inputs and expression patterns of neuromodulatory receptors also distinguish cerebellar regions (Cerminara et al., 2015). While it is clear that norepinephrine (NE) regulates cerebellar output, the mechanistic details of neuromodulatory effects for other amines remain poorly understood (Basile and Dunwiddie, 1984; Carey and Regehr, 2009; Lanore et al., 2019; Lippiello et al., 2015). Several previous reports posit the expression of dopamine type 1 receptor (Drd1a) within the granular layer of the cerebellum (Locke et al., 2018; Panagopoulos et al., 1993). Additionally, several groups have previously reported dopaminergic projections from the substantia nigra pars compacta (SNc) and the ventral tegmental area (VTA) targeting the cerebellar cortex of rats and monkeys (Melchitzky, 2000; Panagopoulos et al., 1991). Yet, recent work in mice did not find evidence for projections from midbrain dopaminergic nuclei to the cerebellum (Giovannucci et al., 2017). Another potential source of dopamine to the cerebellum is from a subset of tyrosine hydroxylase (TH) positive Purkinje (Pkj) cells. Vestibulo-cerebellar Pkj cells express tyrosine hydroxylase, the rate-limiting enzyme in the classical dopamine (DA) synthesis pathway (Abbott et al., 1996; Chung et al., 2009, 2010; Huang et al., 2016; Sawada et al., 2004; Takada et al., 1993). One prior report details dendritic release of DA by Pkj cells onto their own dendrites, expressing dopamine type 2 receptor (Drd2) (Kim et al., 2009). It is possible that these Pkj cells could also be the source of dopamine to local UBCs expressing Drd1 receptors. A third potential source of cerebellar DA is the locus coeruleus, recently demonstrated to release dopamine as well as norepinephrine in the hippocampus (Kawahara et al., 2001; Kempadoo et al., 2016; Takeuchi et al., 2016). The proposed mechanism of action for this dual amine

91 co-release is incomplete conversion of dopamine to norepinephrine in the vesicles. If incomplete conversion
92 also takes place in the cerebellum, then DA release could enhance activity levels in the UBC network or
93 coordinate the timing of their activity.

94 Altogether, previous research is consistent with the possibility of cerebellar DA signaling, but many unknowns
95 remain. Here, using a combination of anatomical characterization, electrophysiology, two-photon laser
96 scanning microscopy and glutamate photolysis, along with optogenetics and DA sensor imaging, we resolve
97 this uncertainty by characterizing the expression of Drd1a receptors in the cerebellar cortex, defining the role
98 of these receptors and the function of Drd1a-positive UBCs within cerebellar circuits, and revealing the
99 source of cerebellar DA.

100

101 **RESULTS**

102 **Expression of Drd1a receptors in UBCs of lobules IX/X**

103 Analysis of Drd1-EY262-Cre;tdTomato expression in the cerebellar cortex reveals numerous small
104 tdTomato+ (tdT) cells distributed across the cerebellar granular layer (Figure 1A), enriched in lobules IX and
105 X of the cerebellar vermis, lobules VIb and VII, and the paraflocculus. These regions of the cerebellum are
106 known to contain many UBCs. Confocal images confirm that cerebellar tdT+ cells possess the morphological
107 features of UBCs: a single large dendritic brush and a medium sized soma relative to granule cells (Figure
108 1B). All tdT+ cells in the cerebellum were positive for nuclear protein Eomesodermin (Tbr2), a known marker
109 for all UBCs (Englund, 2006). However, only 35% of Tbr2+ UBCs expressed tdT, suggesting that only a
110 subpopulation of UBCs express tdT (Figure 1C, Figure S1A). Since two primary classes of UBCs have been
111 previously characterized (Kim et al., 2012; Zampini et al., 2016), we relied on known immunohistochemistry
112 markers to characterize tdT+ UBCs. The majority of tdT+ neurons express mGluR1 (Figure 1D) (71%, n=3
113 mice, 621 cells). The mGluR1+ and tdT+ populations do not completely overlap, as only 65% of mGluR1+
114 UBCs express tdT. Very few tdT+ UBCs belong to calretinin+ (CR) type: 5.6% of tdT+ UBCs express CR,
115 and 13.6% of CR+ UBCs express tdT (Figure 1E). Given these data, we infer that in the Drd1-Cre;tdT cross,
116 all cerebellar tdT+ cells are UBCs, and that these tdT+ UBCs are a subset of the total UBC population, mostly
117 comprised of mGluR1+ ON UBCs. A prior report using a different Drd1-cre mouse line reported the
118 expression of Drd1 receptors in deep cerebellar nuclei (Locke et al., 2018). In contrast, we do not see
119 expression of tdT in the cerebellar nuclei in this transgenic cross. Because Cre recombinase lines can show
120 developmentally regulated or ectopic expression patterns, next we evaluated whether tdT+ UBCs contain
121 Drd1a receptors using fluorescent in situ hybridization (FISH) to label *tdT* and *Drd1a* mRNA transcripts. High
122 density tdT transcripts were used to create ROIs in a custom FIJI pipeline (Schindelin et al., 2012; Schneider
123 et al., 2012) to examine colocalization with *Drd1a* transcripts. We found that up to 76% of *tdT*+ (Figure 1F)
124 UBCs expressed *Drd1a* transcripts in low abundance (n=4 animals, 2553 cells) across an age range from

P20s to P60s (Figure S1B-C). The density of *Drd1a* puncta was 40-fold enriched in the volume of *tdT*+ ROIs, compared to regions outside the cell bodies (Figure S1D). These data suggest that tdT+ UBCs express modest levels of Drd1a receptors.

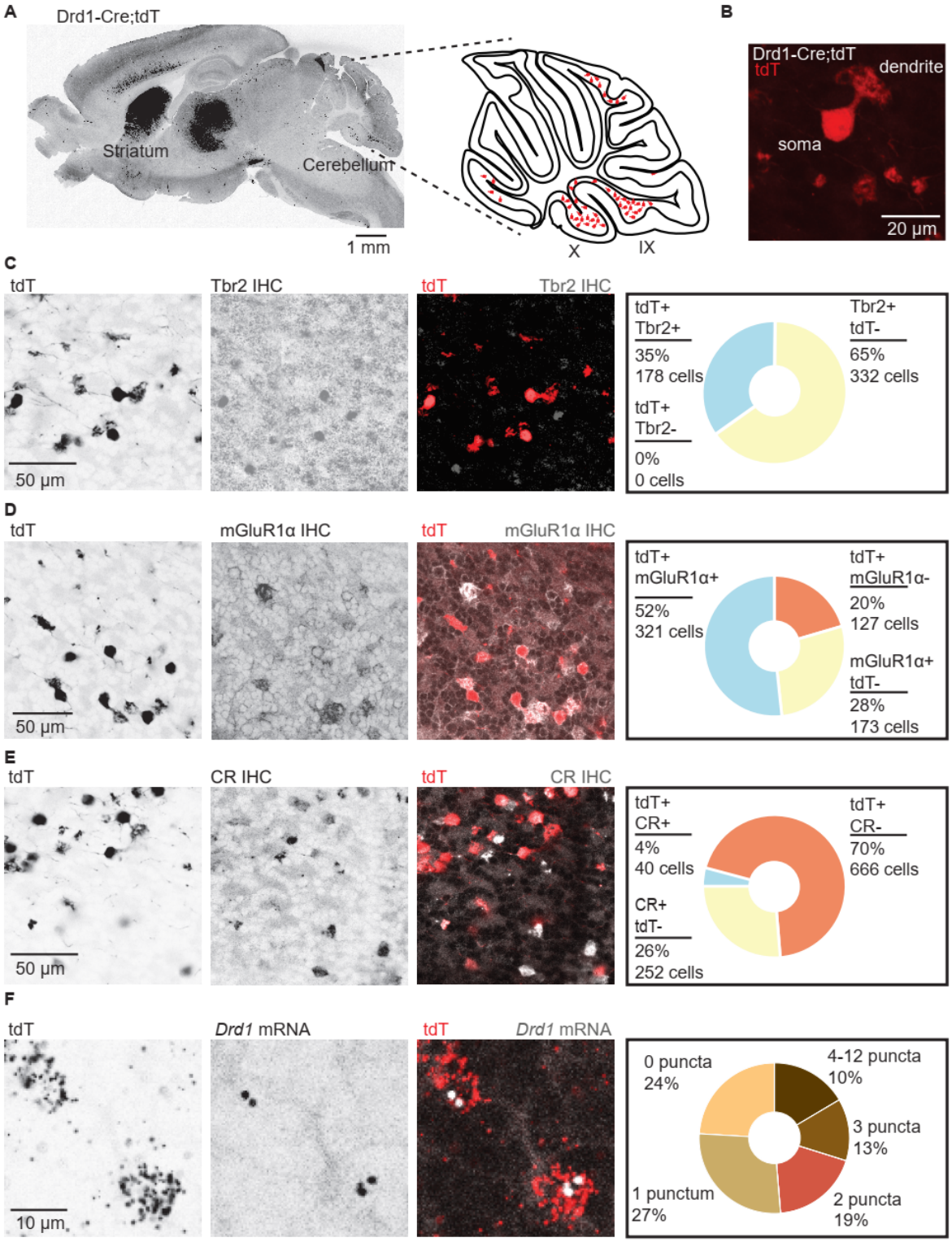

Figure 1: Drd1 receptors are expressed in mGluR1+ UBCs.

130 **A.** *Left*: A whole brain parasagittal section from a Drd1-Cre;tdT reporter cross. *Right*: A cartoon view of a parasagittal
131 slice of the cerebellar vermis. TdTomato expressing UBCs are abundant in lobules IX/X of the vermis. Scale bar, 1 mm.

132 **B.** A confocal image of a tdT+ UBC in the cerebellum of a Drd1-Cre mouse, showing the characteristic dendritic brush
133 morphology of a UBC. Scale bar, 20 µm.

134 **C.** *Left*: Confocal images of immunofluorescent labeling of Eomesidermin (Tbr2) in lobules IX/X of the cerebellar vermis.
135 *Right*: Pie chart describing overlap of cerebellar tdT+ cells and Tbr2. All tdT+ cells express Tbr2, and a subpopulation
136 (~35%) of Tbr2 cells expresses tdT (n=2 mice, 510 cells). Scale bar, 50 µm.

137 **D.** *Left:* Similar to **C**, but for mGluR1. *Right:* Out of all tdT+ UBCs 71% expressed mGluR1*, 65*% of mGluR1+ UBCs
138 were positive for tdT (n=3 mice, 621 cells). Scale bar, 50 µm.

139 **E.** *Left*: Similar to **C-D**, but for calretinin (CR). *Right:* labeling shows little overlap between CR and tdT+ UBCs, 5.6% of
140 tdT+ UBCS express CR, and 13.6% of CR+ express tdT (n=2 mice, 958 cells). **C-D**. Inverted greyscale, single-channel
141 images; in merged images, red represents tdT signal, grey represents antibody labeling for Tbr2, mGlur1, or CR,
142 respectively. Scale bar, 50 µm.

143 **F.** *Left:* Sample confocal images of FISH, labeling *tdT* and *Drd1a* transcripts in cerebellar UBCs. Inverted greyscale
144 LUT is used for single-channel images. In merged images, red represents tdT signal, grey represents Drd1 labeling.
145 *Right*: The majority (~76%) of tdT+ UBCs express Drd1 transcripts (n=4 mice, 2553 cells). Scale bar, 10 µm.

---

146 **Functional characterization of Drd1a activation in UBCs**

147 To evaluate the consequences of Drd1a receptor activation we used current clamp recordings of tdT+ UBCs
148 (Figure 2A-F, Figure S2A-D). Puff application of selective Drd1 agonist SKF81297 increased the firing rate
149 of tdT+ UBCs (Figure 2C-D) (2.48 Hz increase, 110% increase from baseline, n=13 cells, paired Wilcoxon
150 signed rank test, p=0.02). We also observed increases in resting membrane potential and input resistance
151 (Figure 2F). In a separate data set, we applied SKF81297 in the presence of Drd1 antagonists SKF83566,
152 SCH39166, and SCH23390, blocking the increases in firing rate, membrane potential, and input resistance
153 (Figure 2E-F) (n=13 cells, paired Wilcoxon signed rank test, p=0.49). Puff application of ACSF likewise
154 elicited no changes in firing rate (n=13 cells, paired Wilcoxon signed rank test, p=0.33). Since Drd1 receptors
155 activate $G\alpha_s$-coupled protein cascades (Stoof and Kebabian, 1984; Surmeier and Kitai, 1993), and whole-
156 cell recordings can dialyze cytosolic proteins involved in G protein-coupled receptor (GPCR) signaling (Lahiri
157 and Bevan, 2020), we replicated the effect of Drd1a activation using cell attached recordings (Figure S2E-
158 H) (n=10 cells, paired Wilcoxon signed rank test, p=0.002). Thus, UBCs respond to Drd1a activation with an
159 enhancement in activity, consistent with previous experiments on the effects of Drd1a activation in the
160 striatum and medial prefrontal cortex (mPFC) (Aosaki et al., 1998; Chen et al., 2007; Hernandez-Lopez et
161 al., 1997).

162 Prior research shows an increase in N-methyl-D-aspartate receptor (NMDAR) currents during the activation
163 of Drd1 receptors in mPFC neurons (Chen et al., 2004). Using electrical stimulation of mossy fibers, we found

164 an increase in peak amplitude of NMDAR currents after the flow in of 10 μM SKF81297 (Fig. 2I-K) (15%
165 increase in peak current, n=9 cells, paired t-test, p=0.0251). These experiments were done in the presence
166 of blockers for fast neurotransmission, 1 μM NBQX, 1 μM gabazine, and 1 μM strychnine. In a subset of
167 experiments, we verified that the measured currents were fully blocked by the application of NMDAR
168 antagonist CPP (10 μM, n=3 cells). Since UBCs are recurrently connected, the increase in NMDAR currents
169 may be due to a postsynaptic mechanism or a consequence of increased excitability in presynaptic UBCs.
170 To distinguish between pre- and post-synaptic mechanisms, we used two-photon focal uncaging of MNI L-
171 glutamate to bypass presynaptic terminals (Figure 2L-M) (Kozorovitskiy et al., 2015; Xiao et al., 2018). In the
172 presence of 1 μM MNI L-glutamate for uncaging, 1 μM TTX to silence spontaneous release, and drugs to
173 isolate NMDAR currents, we uncaged glutamate near the dendritic brush of voltage clamped UBCs held at
174 +40 mV. NMDAR mediated currents in response to 1 ms long pulses of 725 nm laser light were compared
175 for experiments with and without 10 μM SKF81297. Current amplitudes increased with Drd1 activation,
176 suggesting a post synaptic mechanism of action (Figure 2 N-O) (51% increase of average amplitude, n=13
177 cells, unpaired t-test, p=0.0068).

178

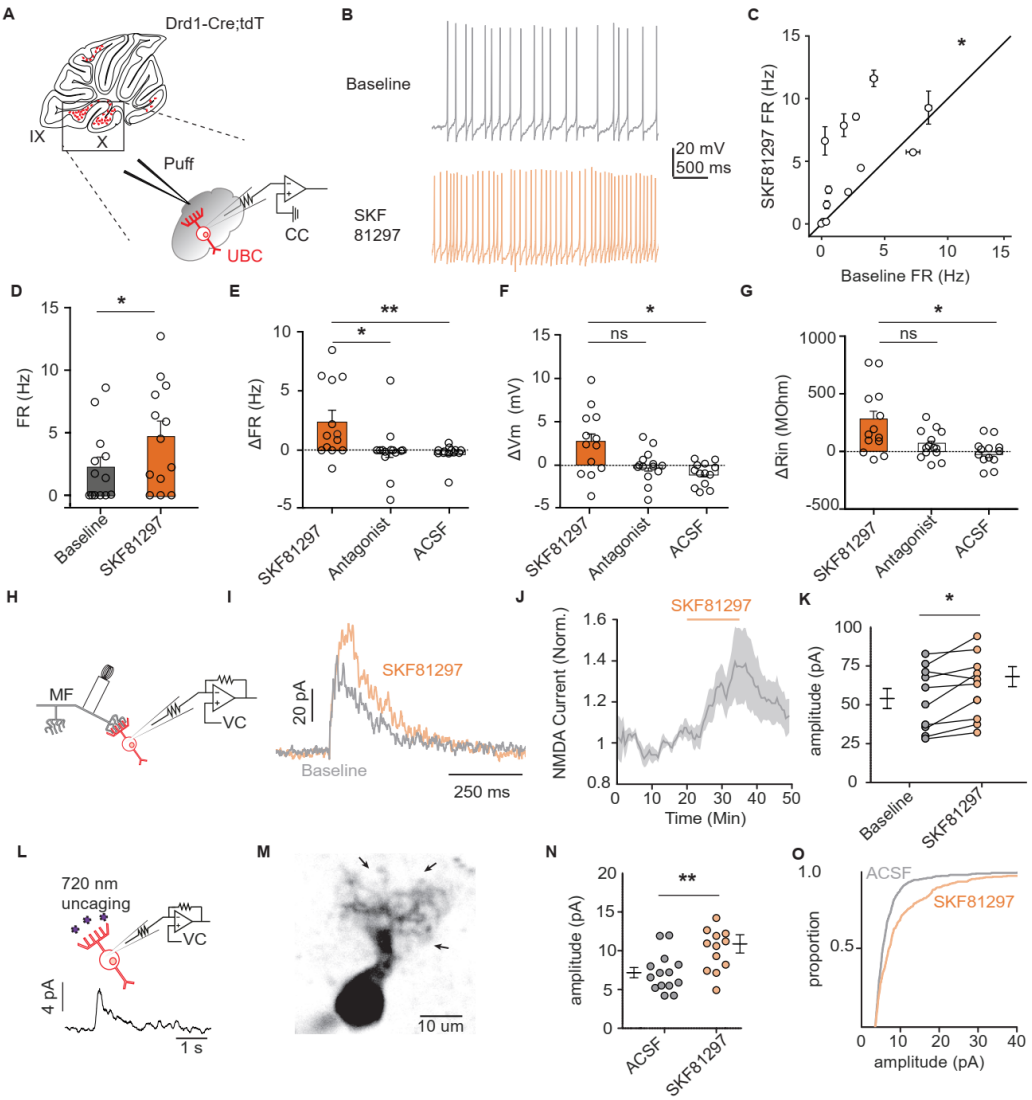

Figure 2. Drd1 activation increases the firing rate and NMDAR currents in UBCs.

A. Diagram of experimental setup with tdT+ UBCs recorded in whole-cell current clamp configuration. Firing rate was measured during baseline period, followed by application of Drd1 agonist SKF81297 (500 μM) with 300 ms-long puffs from a proximally located pipette.

B. Voltage traces from an example cell which increased its firing rate in response to SKF81297 application.

C, D. Group comparison, mean firing rates during the baseline period and application of SKF81297 (n=13 cells, paired Mann-Whitney U test, p=0.02, *p<0.05).

E-G. Changes in firing rate (FR) in **E**, resting membrane potential (mV) in **F**, and input resistance (Rin) in **G**. The SKF81297 group, as in in **C-D**. Comparisons are between three independent data sets. Antagonist group: SKF81297 was applied in the presence of Drd1 blockers 1 μM SKF83566, 1 μM SCH39166, and 1 μM SCH23390 in 0.02% DMSO. ACSF group: puff application ACSF instead of SKF81297 (Kruskal-Wallis test, FR p=0.0044, Vm p=0.0024, Rin p=0.02; Dunn's multiple comparison test, *p<0.05, **p<0.01).

192 **H.** Schematic of experimental setup. Voltage clamp recordings were performed in tdT+ UBCs, paired with stimulation
193 mossy fiber inputs to evoke NMDA receptor mediated currents (inter-trial interval, ITI, 5 seconds), in the presence of
194 blockers for AMPA, GABA and glycine receptors (1 μM NBQX, 1 μM gabazine, 1 μM strychnine).

195 **I.** Sample traces show an increase in NMDAR current amplitudes during the application of SKF81297.

196 **J.** Trace of normalized peak amplitude of NMDAR currents across cells (n=10 cells). Shaded region, SEM.

197 **K.** Summary plot of average evoked NMDAR current amplitudes before and after application of 10 μM SKF81297 (n=10
198 cells, paired t-test, p=0.0251).

199 **L.** *Top:* Schematic of two-photon uncaging MNI-L-glutamate uncaging experiments. TdT+ UBCs were voltage-clamped
200 and imaged using a two-photon laser scanning microscope. Laser pulses at 725 nm directed near the dendritic brush
201 (10-20 mW, 1 ms, 60 s ITI) were used evoked NMDAR mediated currents. *Bottom:* Example current trace.

202 **M.** Two-photon imaging Z- projection of a tdT+ UBC. Arrows represent separate uncaging site locations. Scale bar, 10
203 μm.

204 **N.** NMDAR current amplitudes in ACSF vs 10 μM SKF81297 (unpaired t-test, p=0.0068, **p<0.01). Each data point is
205 the average amplitude of NMDAR currents evoked by glutamate uncaging from one cell (ACSF n=14 cells, SKF81297
206 n=13 cells).

207 **O.** Cumulative distribution of uncaging-evoked NMDAR current peak amplitudes for ACSF and SKF81297 groups.

---

208 **Activation of UBCs preferentially leads to a pause in Pkj cell firing**

209 In order to evaluate the function of Drd1+ UBCs within Lobule X of the cerebellar vermis we transfected Drd1-
210 Cre mice with ChR2-EYFP virus and performed cell attached recordings from Pkj cells (Fig 3A-B). We
211 stimulated UBCs with a train of LED pulses (460 nm, 10 Hz, 50 pulses, 1 ms pulse width). Each pulse caused
212 a small burst of action potentials (2-5 APs). UBCs were more likely to respond with multiple spikes to a pulse
213 at the beginning of the train than at the end (Figure 3B-C). Pkj cells did not significantly alter their average
214 firing rate on trials (15 second) with optogenetic stimulation (Fig 3D). However, in a subset of Pkj cells,
215 stimulation caused a brief pause in firing during the 500 ms period after the beginning of the optogenetic
216 stimulus (Figure 3E). Firing rate was normalized using a z-score. If a cell's firing changed by 0.5 z-score
217 deviation for 500 ms after initial pulse, it was classified as changing. Cells were classified into 'Bursters',
218 'Pausers', or non-responding. The majority of Pkj cells (18/28) did not significantly change their firing rate,
219 ~28% of cells were 'Pausers' (8/28) and 7% of Pkj cells qualified as 'Bursters' (2/28) (Figure 3F-G). In a
220 separate group of cells, we performed tight seal recordings from Pkj cells and measured their responses to
221 5 pulses of optogenetic activation of UBCs. Immediately afterwards, we broke into the cell and recorded
222 EPSCs (-70 mV) and IPSCs (0 mV) in whole cell voltage clamp mode (Figure 3H). We calculated the
223 EPSC/IPSCs charge ratio and plotted it against change in firing rate z-score (Figure 3I). Neurons with lower
224 EPSC/IPSC ratios were more likely to pause after the onset of stimulation, suggesting that in these cells the

225 relatively larger inhibitory current favored the pause. These data demonstrate that simultaneous activation
226 of Drd1+ UBCs induces a decrease in Pkj cell firing.

227

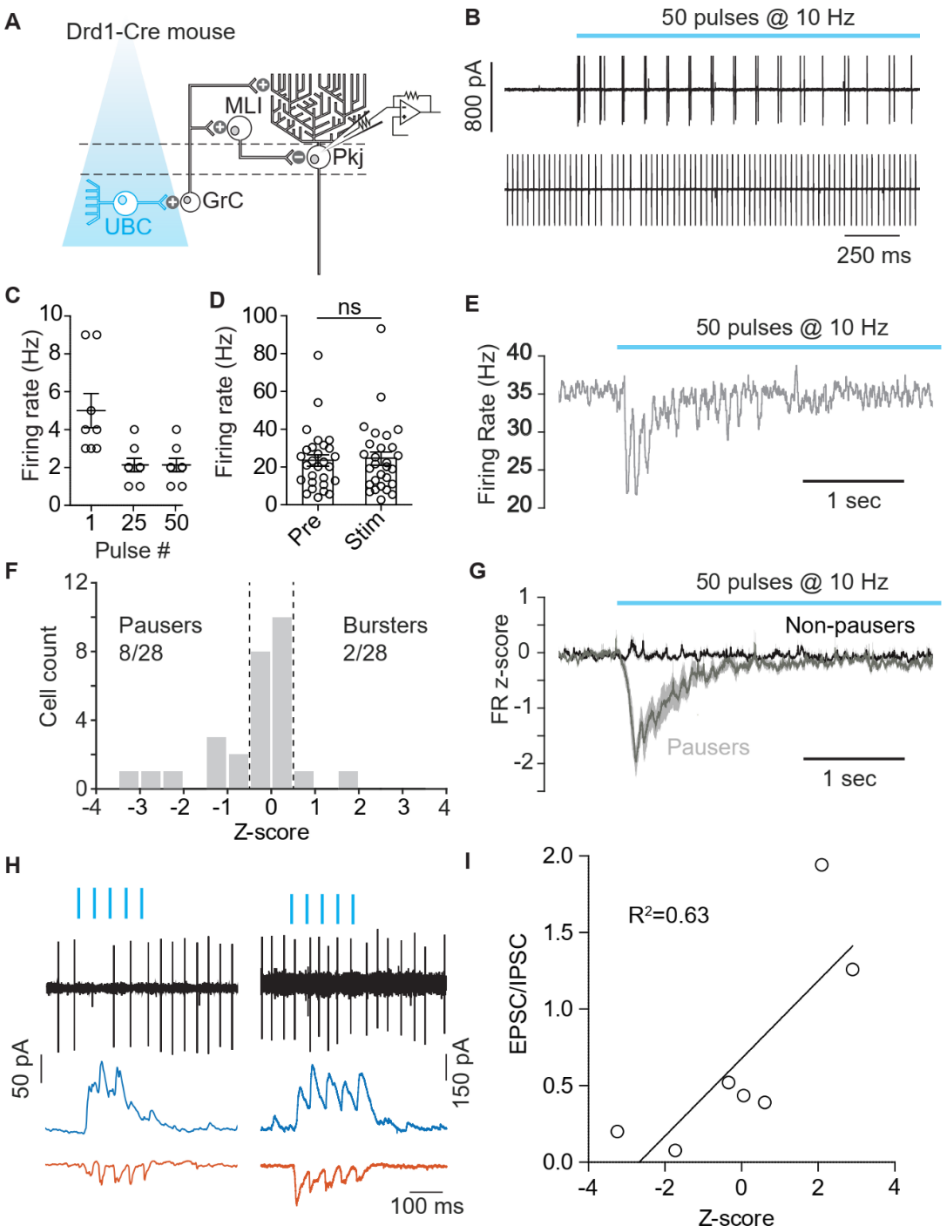

228

229 **Figure 3. Optogenetic activation of UBCs elicits pausing in Pkj cell activity.**

230 **A**. Diagram of experimental setup. Cre-dependent ChR2-EYFP was expressed in UBCs using a Drd1-cre mouse line.
231 Pkj cells were recorded from in both cell-attached and whole-cell voltage clamp configuration.

232 **B.** *Top:* Example trace from a cell-attached recording of a ChR2+ UBC which increased its firing rate during light
233 stimulation (460 nm, 10 Hz, 50 pulses, 1 ms pulse width). *Bottom:* Cell attached recoding from Pkj cell.

234 **C.** The number of action potentials evoked in ChR2+ UBCs by a train of light pulses in response to the 1st, 25th and 50th
235 individual pulse (n=8 cells).

236 **D.** A comparison of average firing rate of Pkj cells for (15 second) trials before optogenetic stimulation of UBCs (Pre)
237 and for trials with optogenetic activation (Stim) shows no significant difference.

238 **E.** The average firing rate (5 trials) of a single Pkj cell during the activation of nearby UBCs. Example cell transiently
239 decreased its firing rate in response to UBC activation.

240 **F**. Histogram of average z-scores of firing rates during the 500 ms period following the first optogenetic pulse. Dashed
241 lines indicate cut-off for categorization of response as either 'Burster' z-score > 0.5 or 'Pauser' z-score < -0.5.

242 **G.** Average z-score of firing rates across cells. 'Pausers' (n=8 cells) indicates data for cells that had z-score < -0.5,
243 'Non-pausers' (n=20 cells) include all other cells. Shaded regions represent SEM.

244 **H.** Cell-attached and postsynaptic current recordings from example Pkj cells; *left* 'Pauser', *right* 'Burster'. Top traces
245 show cell-attached recordings before break-in. After break-in IPSCs (blue trace) and EPSCs (red) were recorded.

246 **I.** Firing rate z-score after optogenetic activation of UBCs plotted against EPSC/IPSC total charge ratio. Data show a
247 correlation between relative inhibitory input and pausing in Pkj cells (Linear regression, p=0.0312).

---

248 **Lobule X Pkj cells directly inhibit UBCs**

249 Previous work showed that in the vestibulo-cerebellum Pkj cells make inhibitory connections with nearby
250 granular cells (Guo et al., 2016). This connection has implications for how Pkj feedback can alter the activity
251 of their own inputs. Given the high density of UBCs in these same regions, we evaluated the possibility of
252 direct synaptic connectivity between Pkj cells and UBCs. We used the Drd1-Cre mouse-line to label UBCs
253 with a flexed GFP reporter virus and selectively activated Pkj cells using a viral vector expressing ChR2-
254 mCherry, driven by the Pcp2 promoter (El-Shamayleh et al., 2017) (Figure 4A). We used epifluorescence to
255 target and patch UBCs with a high chloride ion concentration internal solution. This allowed us to measure
256 IPSCs (Figure 4B) while holding cells at -80 mV. GABAa currents were isolated using pharmacological
257 blockers of AMPA, NMDA, glycine and $GABA_B$ receptors (5 μM NBQX, 2 μM CPP, 1 μM strychnine, 1 μM
258 CGP54626). In order to distinguish between direct inhibition from Pkj cells and any indirect inhibition from
259 nearby Golgi cells, an mGluR2 agonist was included in the bath to silence Golgi cells (2 μM LY354740) (Guo
260 et al., 2016; Watanabe and Nakanishi, 2003).To verify that the LED stimulation protocol effectively drove Pkj
261 cell activity we performed cell attached recordings. We could reliably increase Pkj cell firing rate during light
262 stimulation (n=8 cells, 71 Hz +/- 6.7) (Figure 4C). In UBC voltage clamp experiments we found that 11/24
263 UBCs received short latency synaptic input from Pkj cells (Figure 4D). Cells with successful evoked IPSCs
264 had a per trial success ratio of 0.64 on average (Figure 4D). There was significant variability in the amplitude
265 (91 pA, +/- 24) (Figure 4H) and timing (9.4 ms +/-2.4) (Figure 4E) of optically evoked IPSCs, with some cells
266 exhibiting large currents over the entire stimulation period and others responding with a single large IPSC at
267 the onset of stimulation. However, many UBCs exhibited short latency IPSCs in response to stimulation of
268 Pkj cells (Figure 4H). In a subset of UBCs (n=9 cells) (Figure 4G) we flowed in 10 μM gabazine to ensure

the measured currents were due to GABAa channel opening. Application of gabazine abolished all evoked currents (Figure 4H).

To anatomically confirm direct synaptic contact from Pkj cells to UBCs we performed trans-synaptic tracing with a modified rabies virus CVS-N2c (Reardon et al., 2016) which allowed us to label presynaptic partners of neurons expressing Cre recombinase (Figure 4I). The modified rabies construct cannot enter cells that do not express a TVA receptor and lacks the glycoprotein necessary to replicate into mature virus that can travel pre-synaptically. We infected UBCs with both TVA and the glycoprotein by injecting AAVs (AAV1-CAG-Flex-H2B-eGFP-N2cG and AAV1-EF1α-FLEX-GT) into a Drd1a-Cre transgenic mouse line. After 4-6 weeks of expression, we injected the modified rabies virus into the same region of the cerebellum. The rabies virus travels monosynaptically to the pre-synaptic partners of local UBCs. After 7-8 days of rabies virus expression, we sacrificed the animals and performed histology. The rabies virus includes a transgene for tdTomato and the AAV viruses include a GFP tag. UBCs initially infected with rabies express both GFP and tdT, while cells presynaptic to starter cells express only tdT. Our data (n=4 mice) show presynaptic labelling of Pkj cells, Golgi cells, and vestibular nuclei neurons (Figure 4J-L). Together our electrophysiological recordings and tracing experiments confirm direct presynaptic inhibition from Pkj cells to UBCs.

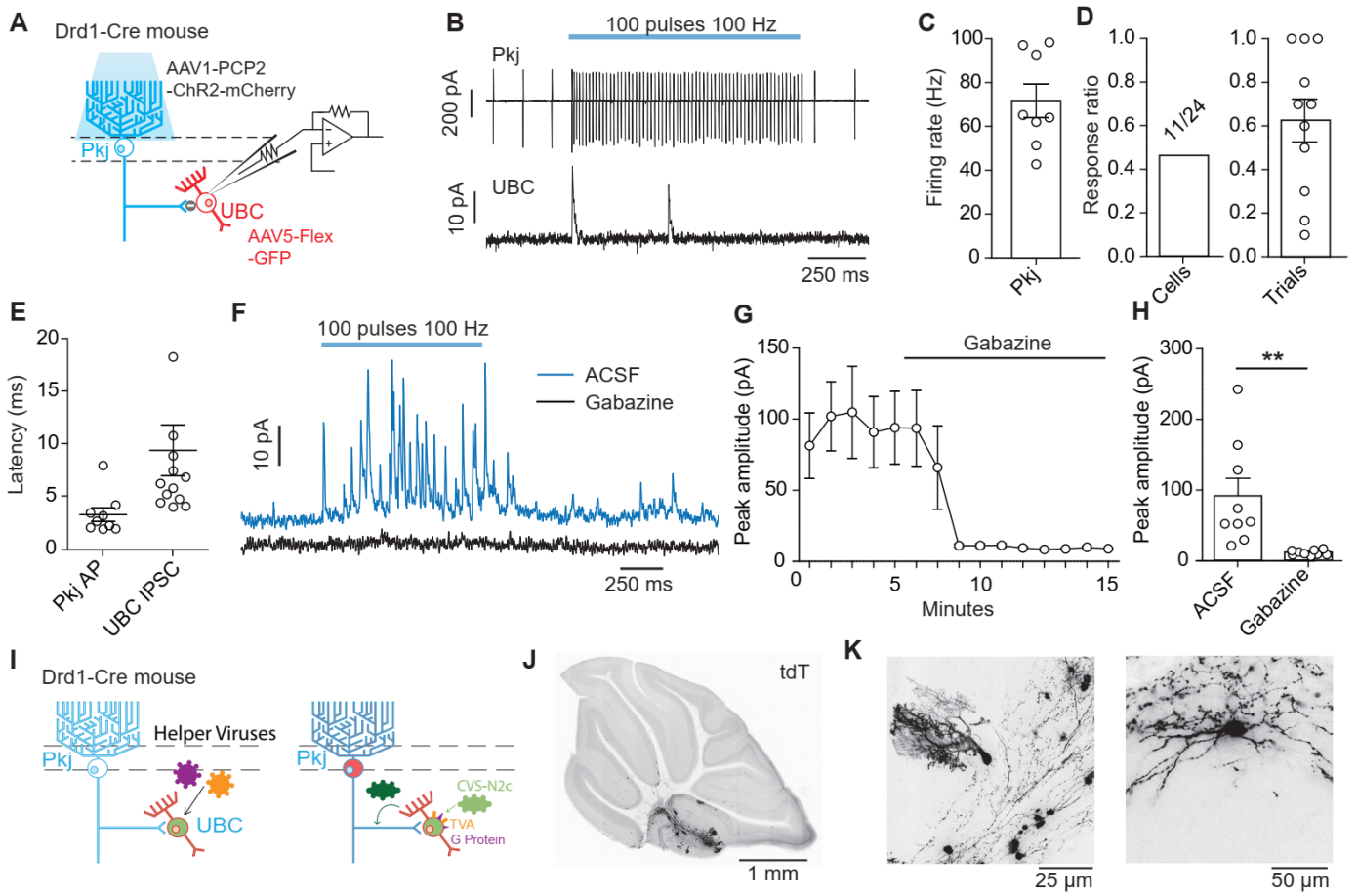

Figure 4. Optogenetic activation of Pkj cells evokes short-latency IPSCs in UBCs.

287 **A**. Diagram of experimental setup. Using a Drd1-Cre mouse line a Cre-dependent GFP was expressed in UBCs, Pkj
288 cells were transfected with AAV-Pcp2-ChR2-mCherry. UBCs recorded in whole-cell voltage clamp configuration.
289 Experiments were done with 5 μM NBQX, 2 μM CPP, 1 μM Strychnine, 1 μM CGP54626, 2 μM LY354740 included in
290 the bath.

291 **B.** *Top:* Example trace from a cell-attached recording of a mCherry+ Pkj cell which increased its firing rate during light
292 stimulation (460 nm, 100 pulses, 100 Hz, 0.5 ms pulse width). *Bottom:* Voltage clamp recording of UBC IPSCs.

293 **C.** Average firing rate of Pkj cells during light stimulation (n=8 cells).

294 **D.** Ratio of successful IPSC responses. *Left (cells):* Represents the ratio of cells in which IPSCs were evoked in
295 response to optogenetic stimulation of Pkj cells (11/24, n=24 cells). *Right (trials):* Ratio of trials in which IPSCs were
296 successfully evoked. Each data point represents the mean from each cell (n=11 cells).

297 **E.** The average latency to the first action potential in a Pkj cell (n=9 cells) or first evoked IPSC in a UBC (n=11 cells).
298 Latency is calculated from the time of first pulse of 460 nm LED light. Each data point represents the mean (5-10 trials)
299 from one cell.

300 **F.** Example data from one UBC shows a near complete inhibition of IPSCs (blue trace) after the application of 10 μM
301 gabazine (black trace).

302 **G.** Time course of reduction of IPSC amplitude by gabazine (n=9 cells).

303 **H.** Population data comparing peak IPSC amplitude before and after gabazine application (n=9 cells, paired t-test,
304 p=0.001).

305 **I.** Cartoon of viral expression for trans-synaptic modified rabies tracing. Helper virus expressing two Cre dependent
306 constructs, TVA receptors and glycoprotein. After 4-6 weeks of helper virus expression in UBCs we injected modified
307 rabies (CVS-N2cΔG). The rabies virus only enters UBCs expressing the TVA receptor. Once expressed in a UBC along
308 with the glycoprotein, the virus can create a functional capsid and travel pre-synaptically.

309 **J.** Representative image of sagittal cerebellar slice. Cells infected with rabies virus are labelled with tdTomato.

310 **K.** Example cells presynaptic to Drd1+ UBCs labelled with tdTomato. *Left:* Pkj Cell, Right: Golgi cell.

---

311 **Defining the source of cerebellar DA**

312 Three TH+ populations are poised to serve as the source of DA to the cerebellum based on prior data: the
313 midbrain dopaminergic cells of the Substantia Nigra pars compacta (SNc) and the Ventral Tegmental area
314 (VTA), local TH+ Pkj cells of the cerebellum, and nearby locus coeruleus (LC) neurons that release DA as
315 well as norepinephrine in other brain regions. First, to evaluate whether Drd1+ UBCs could receive inputs
316 from midbrain DA neurons, we carried out retrograde tracing from the vestibulo-cerebellum in a Dat-Cre;tdT
317 mouse cross. We found no support for the existence of this projection (Figure 5A-C), despite the abundance
318 of Dat-Cre;tdT axonal fibers in the cerebellum (Figure 5B, inset). Retrograde labelling confirmed that these
319 tdT+ axons originate from a pre-cerebellar brainstem nucleus, the lateral reticular nucleus (LRN), and not

320 the SNc/VTA. LRN neurons are glutamatergic, forming mossy fiber rosettes within the cerebellum
321 (Rajakumar et al., 1992; Wu et al., 1999). There are no prior reports of LRN expressing proteins required for
322 DA synthesis or packaging. Next, using FISH and antibody labeling, we confirmed previous reports of TH
323 expression in Pkj cells of vermal lobules IX and X (Figure 5D-F) (Austin et al., 1992; Sakai et al., 1995;
324 Takada et al., 1993). Despite the presence of *Th*, these neurons lacked the transcripts for Dopa
325 Decarboxylase (*Ddc*), the enzyme responsible for converting L-DOPA to dopamine (Figure 5E-F) (n=2 mice,
326 163 cells). Similarly, we found minimal expression of vesicular monoamine transporter type 2
327 *(Vmat2/Slc18a2*) or dopamine active transporter *(Dat/Slc6a3*), in contrast to *Th*+ neurons of the SNc (Figure
328 5G). Thus, DA release from TH+ Pkj cells is unlikely. Exclusion of the first two hypothesized DA sources left
329 the nearby monoaminergic LC as a candidate. To verify that the LC projects specifically to cerebellar regions
330 enriched in Drd1+ UBCs, we used a TH-FLPO mouse line. We injected a retrograde AAV (rAAV2-fDIO-Cre-
331 EGFP) into lobules IX/X and found EGFP+ LC neurons (Figure 6A-B). Consistent with TH expression in
332 lobule IX/X (Figure 5D), local Pkj cells were also labelled by the injection. The SNc and VTA did not express
333 EGFP, further confirming the absence of a TH+ projection from VTA/SNc. We performed the complementary
334 anterograde experiment, injecting AAV1-Flex-FRT-ChR2-mCherry into the LC, and detected labelled axons
335 across the entire cerebellum, including in the regions which contain Drd1+ UBCs (Figure 6C). Given these
336 data, the most likely source of dopamine to Drd1+ UBCs is the LC.

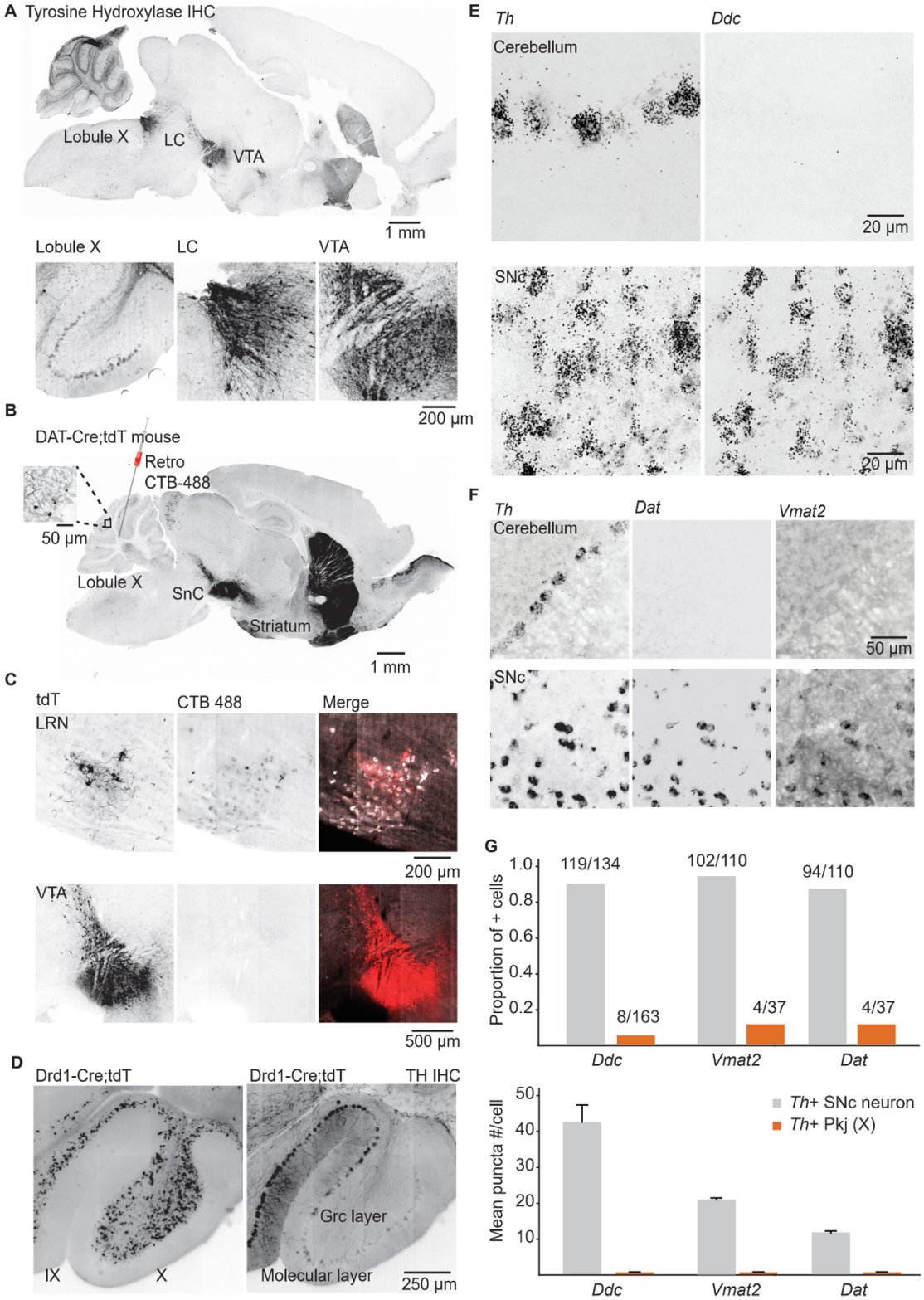

Figure 5. Interrogating potential dopamine sources for cerebellar lobules IX/X.

A. *Top:* Parasagittal slice of a mouse brain immunolabelled for tyrosine hydroxylase (TH). Three hypothesized sources of dopamine include Purkinje cells in lobule X of the vermis, locus coeruleus neurons, and VTA DA neurons. Scale bar, 1mm. *Bottom:* Close-up of regions of interest. Scale bar, 200 µm.

342 **B.** Example retrograde labeling experiment with CTB-488 injected into the cerebellum of a Dat-Cre;tdT reporter mouse
343 (n=3 mice). Scale bar, 1 mm. *Inset:* TdTomato expressing cerebellar fibers have a morphology consistent with mossy
344 fiber terminals and are restricted to the granule layer. Scale bar, 50 µm.

345 **C.** Close-up images from a retrograde CTB-488 injection. No labeling is observed in the tdT+ neurons in the ventral
346 tegmental area (VTA), in contrast to tdT+ neurons in the lateral reticular nucleus (LRN), a glutamatergic pre-cerebellar
347 brainstem nucleus. Scale bars, 200 µm and 500 µm.

348 **D.** Example images from the cerebellum of Drd1a-Cre;tdT mouse, immunolabelled for TH, showing TH+ Pkj cells and
349 tdT+ UBCs in lobules IX/X of the cerebellar vermis. Scale bar, 250 µm.

350 **E.** *Top*: Confocal images of FISH labeling for *Th* and *Ddc* transcripts in Pkj cells in lobule X. *Bottom*, images of SNc
351 neurons co-labeled for *Th* and *Ddc* transcripts (n=2 mice). Scale bar, 20 µm.

352 **F.** Comparison of TH+ Pkj cells and SNc neurons co-labeled for dopamine active transporter *(Dat)* and vesicular
353 monoamine transporter type 2 *(Vmat2)* (n=2 mice). Scale bar, 50 µm.

354 **G.** Quantification of transcripts involved in synthesis and release of DA. *Top*: Few TH+ Pkj cells express transcripts for
355 *Ddc, Vmat2* or *Dat*. *Bottom*: The few TH+ Pkj cells that express *Ddc, Vmat2*, and *Dat* express low transcript numbers
356 in comparison to SNc neurons (n=2 mice). Grey bars represent counts from SNc DA neurons, red bars represent *Th*+
357 Pkj cells.

---

358 To obtain evidence of functional DA release in the cerebellum, we turned to optical dopamine sensors that
359 can directly measure dopamine release with more sensitivity than fast scan cyclic voltammetry and higher
360 temporal resolution than microdialysis (Patriarchi et al., 2018; Sabatini and Tian, 2020). We injected a Cre-
361 dependent version of $GRAB_{DA2h}$ AAV (Sun et al., 2018, 2020) into lobule IX/X of the cerebellum of Drd1a-
362 Cre animals. We then paired electrical stimulation of cerebellar cortical inputs with 2-photon imaging of
363 $GRAB_{DA2h}$ fluorescence in UBCs in the acute slice (Figure 6D). We found that electrical stimulation of inputs
364 to lobule X (50 stimuli, 50 Hz) elicited an increase in $GRAB_{DA2h}$ fluorescence in UBCs (Figure 6F). This
365 increase could be blocked by bath application of Drd2 antagonist, as expected for this sensor (Figure 6G) (1
366 µM L-741,626, n=10 cells, 4.88-fold reduction in peak amplitude, paired t-test, p=0.002). The electrical
367 stimulation protocol lacks specificity, activating all inputs into lobule X. To selectively activate the putative DA
368 inputs, we crossed Drd1-Cre and TH-FLPO mouse lines to express $GRAB_{DA2h}$ in UBCs and ChR2 in TH+
369 inputs to the nodulus. We imaged $GRAB_{DA2h}$ fluorescence in UBCs in the acute slice while optogenetically
370 activating LC axons (20 pulses, 39 Hz, 2 ms pulses, 460 nm). In each experiment, the absence of TH+ Pkj
371 cell labeling was confirmed to ensure selective LC targeting without overflow of ChR2 expression into the
372 cerebellum. We found time-locked increases of $GRAB_{DA2h}$ fluorescence in UBCs in response to optical
373 stimulation, for a subset of UBCs (5/20 cells) (Figure 6I). Optically evoked $GRAB_{DA2h}$ transients were not as
374 reliable as electrical stimulation experiments, with a success rate of ~20%. Altogether, these electrical and
375 optical imaging experiments suggest that LC axons release neuroactive molecules that activate dopamine
376 receptors in the cerebellum.

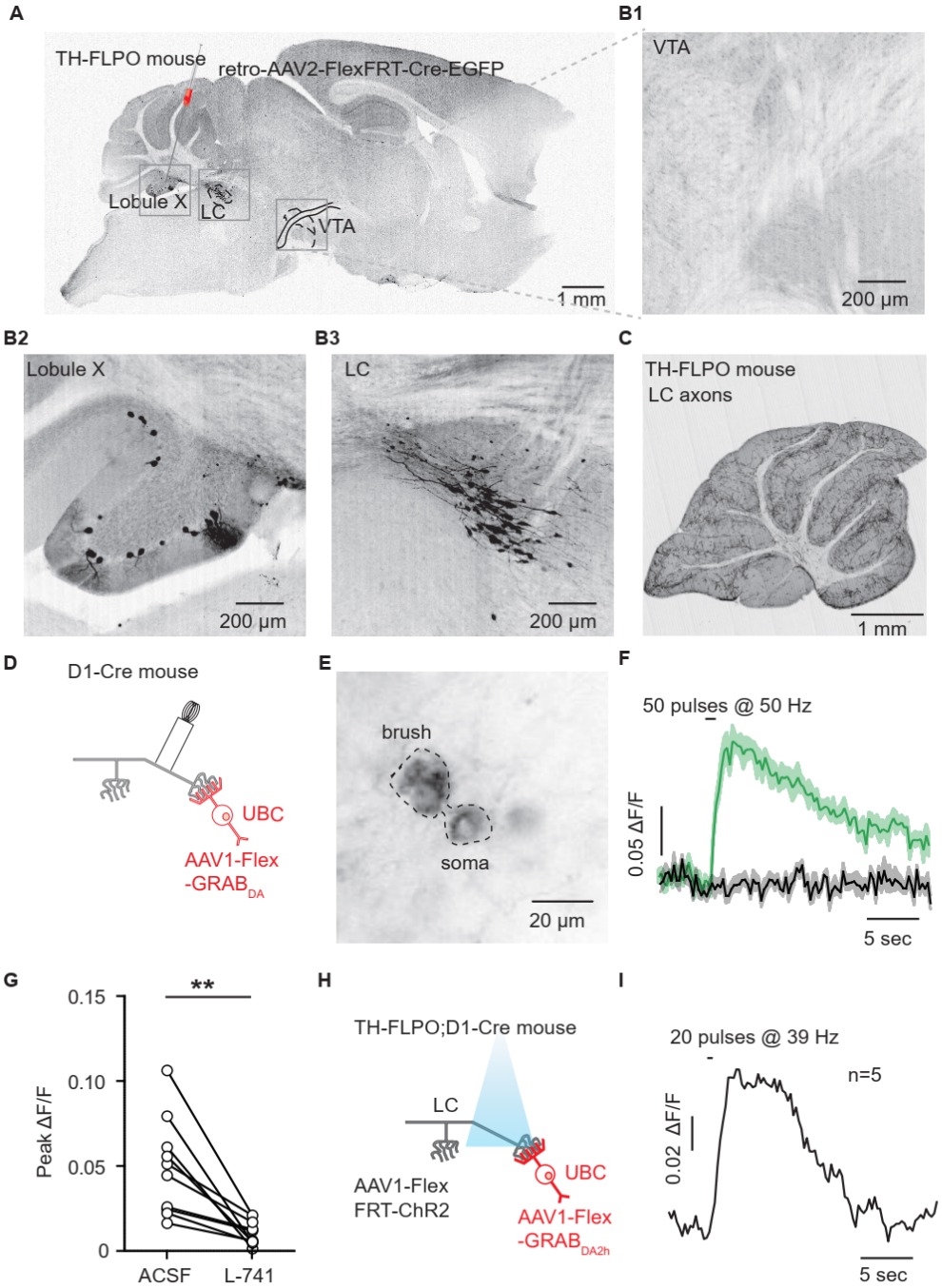

Figure 6. LC fibers target the cerebellum to activate an optical dopamine sensor GRAB$_{DA2h}$.

A. Parasagittal section from a TH-FLPO mouse injected with retrograde FLP-dependent virus expressing GFP (retro-AAV2-FlexFRT-Cre-EGFP). Lobule X of the vermis, LC, and the SNc are outlined. Scale bar, 1 mm.

B1-3. Close-up of outlined regions in panel A. No GFP labeling of VTA/SNc neurons was observed, in contrast to LC neurons and local TH+ Pkj cells that were retrogradely labeled by GFP (n=2 mice). Scale bar, 200 µm.

385 **C.** Anterograde labeling of axons from the LC to the cerebellum. Image from an injection of AAV1-FLEX-FRT-ChR2-
386 mCherry into the LC shows axons spreading broadly across all layers of the cerebellum (n=2 mice). Scale bar, 1 mm.

387 **D.** Schematic of experimental setup, Cre-dependent $GRAB_{DA2h}$ expressed in UBC, with a monopolar electrode placed
388 in the white matter of Lobule X.

389 **E.** Two-photon image of UBCs expressing Cre-dependent $GRAB_{DA2h}$ in a Drd1-Cre cerebellum.

390 **F.** Sample trace from one cell (5 trial average) in response to electrical stimulation before and after application of Drd2
391 antagonist (1 μM L-741,626). Shaded regions, SEM.

392 **G.** Group data of peak amplitude of ΔF/F in response to 50 Hz stimulation of axonal cerebellar input before and after
393 flow in of Drd2 antagonist (1 μM L-741,626) (n=10 cells, paired t-test, p=0.002, **p<0.01).

394 **H.** Experimental design using dual virus injection to express ChR2 (FLP-dependent) in LC axons and $GRAB_{DA2h}$ (Cre-
395 dependent) in UBCs. Light pulses were delivered with 460 nm LED (2 ms pulse width, 20 pulses, 39 Hz).

396 **I.** A sample trace of change in $GRAB_{DA2h}$ fluorescence in response to optical activation of ChR2+ LC axons. Across
397 several experiments, 5/20 cells responded to optogenetic activation (6 acute slices, n=2 mice).

---

398 **DISCUSSION**

399 In this study, we characterized the expression and function of Drd1 receptors in mGluR1+ (ON type) UBCs
400 of the cerebellar vermis. We leveraged the ability to genetically target these UBCs for electrophysiological
401 recording using the Drd1-Cre mouse line. We found changes in spontaneous activity of UBCs and their
402 NMDAR mediated currents by combining electrophysiological recordings with 2-photon glutamate uncaging
403 and 2-photon imaging. These effects are consistent with the literature on Drd1 receptor function across
404 multiple brain regions (Chen et al., 2004, 2007; Lahiri and Bevan, 2020). We found that UBCs receive direct
405 inhibition from local Pkj cells, and that the activation of UBCs can significantly alter the firing rate of Pkj cells,
406 forming a closed reciprocal loop. We evaluated several distinct hypotheses for the source of dopamine to the
407 cerebellum and found that neurons in the LC project to cerebellar regions enriched in Drd1+ UBCs.
408 Optogenetic activation of LC fibers elicited strong responses in the dopaminergic optical sensor $GRAB_{DA2h}$
409 which is consistent with local DA co-release from TH+ LC inputs. These findings expand our knowledge about
410 neuromodulation in the cerebellum and reveal a new function for LC inputs in cerebellar processing.

411 While the cerebellum is known to receive dense innervation from several neuromodulatory nuclei (Li et al.,
412 2014; Nelson et al., 1997; Schweighofer et al., 2004), questions about the role of these neuromodulators
413 have been difficult to address. The function of DA in the cerebellum has been particularly elusive due to
414 disagreement about the location of receptors and potential sources of DA (Hurley et al., 2003; Kim et al.,
415 2009; Locke et al., 2018; Mansour et al., 1991). To evaluate cerebellar DA receptor expression, we used a
416 combination of transgenic tools and FISH, characterizing the distribution of *Drd1a* mRNA in mGluR1a+ UBCs
417 from the Drd1-EY262-Cre line crossed to a tdTomato reporter. Most Drd1 UBCs express a low amount of

418 *Drd1* transcripts. Since UBCs are compact cells with small somato-dendritic compartments, a low transcript
419 number of *Drd1a* mRNA could produce sufficient receptor levels to impact UBC activity.

420 We evaluated the consequences of Drd1 activation by recording the activity of Drd1+ UBCs before and after
421 activating Drd1 receptors. Most tdT+ UBCs (70%) increase their firing rate in response to Drd1 activation, as
422 has been reported for Drd1 mediated effects on striatal spiny projection neurons (Lahiri and Bevan, 2020).
423 Quiescent neurons characterized by hyperpolarized resting membrane potential did not initiate activity in
424 response to pharmacological stimulus. This observation suggests several non-exclusive possibilities. First,
425 Drd1 receptor mediated depolarization may be insignificant in some UBCs. Second, the effect of Drd1
426 agonism is, at least in part, dependent on ionic currents that are not active below a certain membrane
427 potential threshold. Third, the effect of Drd1 activation could be unable to overcome the ionic currents that
428 regulate the 'down' state in UBCs. One intriguing possibility is that previously described bimodal states in
429 UBCs (Diana et al., 2007) map onto distinct responses to neuromodulatory inputs.

430 Based on previous literature on the mechanisms of dopamine neuromodulation in the mPFC (Chen et al.,
431 2004), we evaluated NMDAR-mediated currents in response to mossy fiber electrical stimulation, finding an
432 increase in NMDAR currents in the presence of a Drd1 agonist. We relied on two-photon glutamate uncaging
433 and imaging combined with electrophysiology to confirm the postsynaptic mechanism for Drd1-dependent
434 increase in NMDAR currents in UBCs. As compact neurons, UBCs have relatively small total NMDA currents,
435 yet this increase could have wide ranging consequences for cellular activity. The enhancement in protein
436 kinase A (PKA) activity, a consequence of Drd1 receptor activation, can promote calcium flux through
437 NMDARs (Skeberdis et al., 2006). Increased calcium flux through NMDARs could be analogous to the
438 increases in striatal L-type voltage gated calcium currents in response to Drd1 receptor activation, with regard
439 to calcium-dependent intracellular signaling cascades (Hernandez-Lopez et al., 1997; Surmeier et al., 1995).
440 Drd1 effects, mediated by $G\alpha_s$-coupled pathways, have diverse impacts on neuronal channels, raising the
441 likelihood that other currents in UBCs are also altered by Drd1 activation. Of special note for Drd1+ UBCs,
442 DA might enhance mGluR1 mediated transient receptor potential channel (TRPC3) currents (Sekerková et
443 al., 2013), as has been previously demonstrated for striatal cholinergic interneurons (Chuhma et al., 2018).
444 If so, this mechanism would have synergistic effects with NMDA receptor-mediated current enhancements.

445 The discovery of Drd1 receptors in UBCs created an opportunity to define their function within vestibulo-
446 cerebellar circuits using the Drd1-Cre mouse line. The results from our experiments demonstrate that
447 optogenetic activation of UBCs can induce pausing in local Pkj cells. This effect is likely explained by
448 differential activation of On and Off parallel fiber beams to Pkj cells (Dizon and Khodakhah, 2011). 'On beam'
449 parallel fibers, originating from the granule cells directly below a Pkj neuron, make excitatory synapses onto
450 that Pkj cell. While granule cells that are not directly below a Pkj cell form 'Off beam' parallel fibers, which
451 will not contact that Pkj cell directly. However, 'Off beam' parallel fibers activate molecular layer interneurons,
452 which then inhibit adjacent Pkj cells. Due to the spatial distribution of UBCs in the granular layer and our

453 whole-field optogenetic activation protocol, 'Off beam' parallel fiber excitation is favored in our slice
454 configuration. How likely is it that similar concurrent activation of UBCs occurs *in vivo*? ON UBCs, those
455 expressing mGluR1 receptors, fire bursts of action potentials in response to glutamate release (Zampini et
456 al., 2016). Since the majority of Drd1+ UBCs are mGluR1+, they would likely burst fire in response to mossy
457 fiber input. Due to recurrent connections between UBCs, a burst of action potentials in one ON UBC could
458 cause a chain of activity leading to near simultaneous granular layer activity across a large area. On the
459 other hand, if ON UBCs selectively project to OFF UBCs simultaneous activity arising from the activity of a
460 few ON UBCs would be unlikely. Future experiments are necessary to refine specific patterns of connectivity
461 among vestibulo-cerebellar UBCs. We also took advantage of the Drd1-Cre mouse line to interrogate the
462 presynaptic inputs to UBCs. Recent work has found that Pkj cells in the vestibulo-cerebellum synapse onto
463 nearby granule cells (Guo et al., 2016), but it remains unknown whether local UBCs receive feedback input
464 from Pkj cells. Notably, Pkj cell feedback to granule cells appears to be restricted to the vestibular regions of
465 the cerebellar cortex, with important implications for the recurrent activity of Pkj cells in these lobules. Our
466 findings expand the recurrent vestibulo-cerebellar circuit to include UBCs. Since UBCs diverge in the granular
467 layer, any circuit level effects from feedback inhibition via Pkj cells is likely to be amplified.

468 We next investigated three potential non-exclusive sources of DA to the cerebellum: the SNc/VTA, local TH+
469 Pkj cells, and the LC. Consistent with some (Wagner et al., 2017), but not all previous reports (Melchitzky,
470 2000; Panagopoulos et al., 1991), we found no evidence of projections from the SNc/VTA. While we were
471 able to confirm TH expression in nearby Pkj cells (Locke et al., 2020; Takada et al., 1993), FISH analyses of
472 *Ddc, Vmat2*, and *Dat* in the *Th*+ neurons confirm that these neurons lack the molecular machinery for
473 releasing DA. Previous work has found that while Pkj cells expressed TH, this protein is maintained in an
474 unphosphorylated state, unable to produce L-DOPA (Lee et al., 2006; Sawada et al., 2004). Given the
475 absence of L-DOPA synthesis, the function of TH in Pkj cells currently remains unknown. However, there
476 are other neuronal classes that express TH but lack complementary proteins for DA release, including a
477 subpopulation of olfactory bulb neurons (Chand et al., 2015), striatal GABAergic interneurons (Weihe et al.,
478 2006; Xenias et al., 2015), and cortical interneurons (Asmus et al., 2008). As the final potential source of DA
479 for UBCs, we evaluated the LC, known to project to the cerebellum (Bloom et al., 1971; Schwarz et al., 2015)
480 and verified here using retrograde AAV injections. Moreover, LC axons have been previously shown to co-
481 release DA and NE in other brain regions. DA released from LC fibers in the hippocampus increases field
482 excitatory postsynaptic currents (EPSCs) and contributes to memory retention (Kempadoo et al., 2016;
483 Takeuchi et al., 2016). In the paraventricular nucleus of the thalamus, DA released by LC axons activates
484 Drd2 receptors to decrease inhibitory inputs (Beas et al., 2018). To test whether LC projections release DA
485 onto UBCs, we used 2-photon imaging of genetically encoded DA sensor $GRAB_{DA2h}$. Either electrical or
486 optogenetic activation of cerebellar LC axons increased $GRAB_{DA2h}$ fluorescence in UBCs. Additional studies
487 are needed to examine whether UBCs also express multiple GPCRs that can be concurrently activated by
488 LC inputs. Although $GRAB_{DA2h}$ is highly specific for DA over NE (DA EC_{50}=0.13 μM, NE EC_{50}=1.7 μM) (Sun
489 et al., 2020), we cannot exclude the possibility of mixed monoamine release from LC axons. Future

experiments using a combination of PKA or cAMP optical sensors (Harada et al., 2017) with pharmacological blockers for NE or DA receptors, could help isolate changes in cAMP due to DA release.

What then could be the functional consequences of DA release onto UBCs? Unipolar brush cells have been found in three distinct brain circuits implicated in the cancelation of self-generated cues due to an animal's movement (Requarth and Sawtell, 2014; Singla et al., 2017; Warren and Sawtell, 2016). Their position in the input layer of the cerebellum means that their activity can significantly alter mossy fiber signals to the cerebellum. In the mouse cerebellum, Drd1 expressing UBCs reside in regions involved in processing vestibular signals and eye movements. However, in larger mammals, UBCs are more widely expressed, suggesting a more diverse role in cerebellar processing. Since we find that Drd1 receptors are expressed predominantly in ON UBCs, DA release from LC axons could coordinate with vestibular mossy fiber inputs to enhance signals arising directly from the otoliths (Balmer and Trussell, 2019).

Leveraging genetic access to a subpopulation of UBCs we have characterized a new recurrent subcircuit between Pkj cells and UBCs, which has the potential to significantly regulate the output of the vestibulo-cerebellum. Altogether, this work expands our knowledge of cerebellar circuitry, resolves longstanding questions about the ability of TH+ Pkj cells to release DA, and points to the LC as the source of DA to the cerebellum.

DATA AVAILABILITY

All data and code generated or analyzed during this study are included in the manuscript and supporting files.

AUTHOR CONTRIBUTIONS

J.E.C and Y.K. conceived the experiments. Anatomical, IHC, and FISH experiments were performed and analyzed by J.E.C., and J.Q. Electrophysiology and two-photon imaging experiments were performed and analyzed by J.E.C. J.E.C. and Y.K. wrote the manuscript, with input from J.Q.

ACKNOWLEDGMENTS

This work was supported by the Rita Allen Foundation Scholar Award, NINDS R01NS107539, Searle Scholar Award, the Beckman Young Investigator Award, William and Bernice E. Bumpus Young Innovator Award, NARSAD Young Investigator and P&S Fund Grant (all Y.K.). J.E.C. was supported as a trainee on an NIH/NINDS institutional training grant (T32NS041234) and with a Ruth Kirschstein National Research Service Award (NRSA) Individual Predoctoral Fellowship (NINDS 1F31NS120736). We thank Dr. Tiffany Schmidt and Northwestern University Biological Imaging Facility for the use of their confocal microscopes, and Lindsey Butler for mouse colony management. We are grateful to Dr. Bernardo Sabatini for the gift of

521 retrograde AAV virus, Dr. Horwitz for the gift of Pcp2 promoter ChR2 AAV, Dr. Yulong Li for sharing the
522 $GRAB_{DA2h}$ virus, and Dr. Raj Awatramani for the TH-FLPO mouse line. We thank Dr. Michael Priest and
523 Samuel Minkowicz for feedback on this manuscript.

524

525 **METHODS**

526 **Materials and Methods**

527 **Mouse Lines**

528 All experiments were performed under the guidelines set by Northwestern University Institutional Animal
529 Care and Use Committee (IACUC). All mice used were on the C57BL/6 background (P20-80). Mice of both
530 sexes were used; sex was tracked for every experiment, and data were analyzed for any differences. Several
531 transgenic lines were used for this project, acquired from Jackson laboratory (Bell Harbor, MA). To visualize
532 Drd1a-positive cells expression we used a heterozygous mouse line with insertion of Cre recombinase at the
533 Drd1a locus (Drd1a-Cre, GENSAT, founder line EY262) (Gong S. Zheng C., 2003). In order to label cells
534 expressing dopamine transporter (DAT) we used knock-in mice expressing Cre recombinase under DAT
535 promoter, B6.SJL-Slc6a3 $^{tm1.1(cre)Bkmn}$/J mice ($DAT^{i\text{-}Cre}$)(Jackson Lab, # 006660) (Bäckman et al., 2006). To
536 label tyrosine hydroxylase positive neurons we used a TH-FLPO developed by the lab of Dr. Raj Awatramani
537 (Poulin et al., 2018). Depending on experiments these Cre lines were either injected with a viral vector or
538 crossed with a floxed tdTomato reporter mouse line (Ai14, Jackson Lab, #007914) (Madisen et al., 2010).
539

540 **Viral vectors**

541 Viruses were acquired from Addgene, UNC vector core, Columbia vector core, Salk Institute, and WZ
542 Biosciences. For stimulation of D1-Cre+ UBCs we injected AAV5-EF1a-DIO-hChR2(H134R)-eYFP-WPRE-
543 hGH (7.2x1012 vg/ml, Addgene, 20298P). For experiments with optogenetic stimulation of Pkj cells we
544 injected AAV1-PCP2-CHR2-mCherry ($7.2x10^{12}$ vg/ml) (El-Shamayleh et al., 2017) and AAV8-Flex-GFP (6.2
545 x1012 vg/ml, UNC vector core). For pseudo-rabies tracing experiments, the viruses were AAV1-CAG-Flex-
546 H2B-eGFP-N2c(G) (2.5×10^{12} gc/ml, Columbia Vector Core), AAV1-EF1α-FLEX-GT (4.3×10^{11} gc/ml, Salk
547 Institute viral vector core), and CVS-N2cΔG tdTomato EnvA (Columbia vector core). For retrograde labelling
548 of TH fibers to the cerebellum, we used AAV2/retro-CAG-fDIO-Cre-EGFP (a gift from the laboratory of
549 Bernardo Sabatini). For anterograde labeling of LC fibers, we injected AAV1-CAG-FLEXFRT-ChR2(H134R)-
550 mCherry (75470, $7x10^{12}$ vg/mL, Addgene). For imaging DA dynamics, we used AAV9-hSyn-DIO-DA4.3,
551 ($GRAB_{DA2h}$, 20191018, $2.7x10^{13}$ vg/mL, WZ Biosciences; plasmid, gift from the laboratory of Yulong Li).
552

553 **Surgical procedures**

554 Animals were anesthetized using an isoflurane vaporizer, with oxygen flow rate maintained at 1.00
555 liter/minute. Induction was done with 2-3% isoflurane and maintenance at 1.5-2%. Tail pinches were used to

556 ensure the effectiveness of anesthesia. Animal was mounted on a stereotaxic frame (David Kopf Instruments,
557 Tujunga, CA), ear bars were inserted, and a chemical depilator as used to expose the skin. Skin was cleaned
558 with iodine followed by alcohol, using aseptic technique. Injections of AAV viral vectors or CTB-488 (Thermo
559 Fisher, C34775) were made using a pulled glass pipette and a UltraMicroPump controller (World Precision
560 Instruments, Sarasota, FL) at a rate of 100 nl/minute. Cerebellar stereotaxic coordinates: AP: -2.5 mm ML:
561 0 mm, from lambda, DV: -2.5 mm from surface of brain. Coordinates for the locus coeruleus: AP: -0.9 mm
562 ML: 0.9 mm, from lambda, DV: -3.2 mm from surface of brain. All animals received an I.P. injection of
563 ketoprofen (0.1 mg/20 g) 0 hours, 24 hours and 48 hours after surgery, with approved post-surgical
564 monitoring. Mice recovered 1 week for retrograde CTB-488 injections and 2-6 weeks for viral vector injections.
565 For modified rabies virus tracing experiments, we allowed the helper viruses to express for 4-6 weeks before
566 injecting rabies virus.
567
568 **Immunohistochemistry**
569 Animals were anesthetized using isoflurane and then transcardially perfused with 4% paraformaldehyde. The
570 brain was extracted and post-fixed at 4ºC in 4% PFA overnight, transferred to phosphate buffered saline
571 (PBS) and stored a 4 ºC. The brain was mounted onto a Leica VT1000s vibratome and 50 µm thick sections
572 were made. Sections were stored in well plates in PBS at 4 ºC. Slices were permeabilized in 0.2% Triton-X,
573 then blocked in 10% BSA with 0.05% Triton-X and incubated in primary antibody for 24-48 hours at 4ºC in
574 0.2% Triton-X. the tissue underwent 3 10-minute rinse steps in PBS and was then incubated in a secondary
575 antibody for 2 hours at RT. Primary antibodies: Rabbit anti-Calretinin (1:500, Swant, CR7697), Mouse anti-
576 mGluR1a (1:500, BD Biosciences, G209-2048), Sheep anti-TH (1:1000, Abcam, ab113), Chicken anti-Tbr2
577 (1:1000, Sigma-Aldrich, AB15894). Secondary antibodies: Goat Anti-Mouse 647 (1:1000, Life Technologies,
578 A-21236), Goat Anti-Rabbit 488(1:1000, Life Technologies A-11034), Donkey-anti-Sheep 647 (1:1000,
579 Thermo Fisher Scientific, A-21448), Goat anti-Chicken IgY (H+L) secondary antibody, Alexa Fluor 488
580 (1:1000, Life Technologies A-11039). IHC samples were mounted onto Superfrost Plus slides (ThermoFisher
581 Scientific, Waltham, MA) dried and cover slipped under glycerol:TBS (3:1) with Hoechst 33342 (1:1000;
582 ThermoFisher Scientific). Slides were imaged at 10X magnification on a slide scanning microscope Olympus
583 VS120 slide scanning microscope (Olympus, Waltham, MA). For IHC quantification slides were imaged using
584 a Leica SP5 confocal microscope (Leica Microsystems) with a 40/63X objective. Z stacks at 2-5 µm step
585 sizes were acquired and images were analyzed in ImageJ (FIJI) (Schindelin et al., 2012).
586
587 **Fluorescence in situ hybridization**
588 Following anesthetization using isoflurane, the mouse was decapitated, and the brain was quickly removed,
589 placed into OCT and frozen on dry ice. Sample was placed in -80ºC freezer for at least 1 night. Tissue was
590 sliced on a cryostat (Leica CM1850) at a thickness of 20 µm and mounted onto Superfrost Plus slides
591 (ThermoFisher Scientific, Waltham, MA). Slices were placed in a slide box and in a Freezer safe Ziploc bag
592 and placed in a -80 ºC freezer overnight before processing. Samples were fixed with 4% PFA in 0.1 M PBS

593 at 4˚C, processed according to RNAscope Fluorescent Multiplex Assay manual for fresh frozen tissue
594 (Advanced Cell Diagnostics, Newark, CA) and coverslipped using ProLong Gold antifade reagent with DAPI
595 (Molecular Probes). Several probes were used including: *tdT (*ACDBio Cat No. 317041*), Drd1a (*ACDBio,
596 Cat No. 406491-C2*), Th (*ACDBio, Cat No. 317621-C2*), Vmat2 (Slc18a2,* ACDBio Cat No. 425331-C3*), Ddc*
597 *(*ACDBio, Cat No. 318681*), Dat (Slc6a3*, ACDBio, Cat No. 315441). Slides were imaged on a Leica SP5
598 confocal in two channels using a 63x objective digital zoom 1.5x with 0.5-micron z steps (512 x 512 pixels).
599 FISH images were analyzed using ImageJ (Schindelin et al., 2012). Images were background subtracted
600 and thresholded. We then used 3D objects counter (Bolte and Cordelieres, 2006) to create a 3-dimensional
601 object. The 3D ROI manager (Ollion et al., 2013) plugin was used to create regions of interest. The tdT
602 channel was used to as a label for UBC soma and to establish ROI. Once ROIs was acquired, we quantified
603 the overlap of signals by counting the number of *Drd1a* puncta within each cell.
604
605 **Acute slice preparation**
606 Mice (P20-60) were deeply anesthetized with isoflurane, followed by a transcardial perfusion using 34ºC
607 (Huang and Uusisaari, 2013) ACSF (artificial cerebrospinal fluid) containing (mM) 127 NaCl, 2.5 KCl, 1.25
608 NaH_2PO_4, 25 $NaHCO_3$, 20 glucose, 2 $CaCl_2$, and 1 $MgCl_2$. After perfusion mice were decapitated, brain was
609 removed, blocked, mounted, and placed into a chamber containing 34ºC ACSF oxygenated with 95% O_2, 5%
610 CO_2. Parasagittal 300 µm cerebellar brain slices were made using a vibratome (Leica VT1200s). Slices were
611 transferred to a holding chamber containing 34ºC ACSF oxygenated with 95% O_2, 5% CO_2, and were
612 incubated for 30 minutes before being cooled to room temperature (22-24ºC).
613
614 **Electrophysiology**
615 All recordings were performed on an acute slice electrophysiology system (Scientifica, UK); neurons were
616 visualized using a 60X water-immersion objective (Olympus, Tokyo, Japan) imaged using a QIClick
617 microscope camera (QImaging, Surrey, Canada), under DIC. Slices were placed in the recording chamber
618 and perfused with oxygenated ACSF at a rate of 2 ml/min, with temperature as noted. For UBC recordings,
619 cells expressing tdTomato in a D1-cre; tdT cross were targeted using epifluorescence illumination from a
620 CoolLED pe4000 system (CoolLED Ltd., Andover, UK). Whole-cell patch electrodes were pulled from
621 borosilicate capillary glass to have a resistance of 2.5-5 MΩ for UBC recordings and 1-2 MΩ for Pkj
622 recordings. All recordings were digitized at 10-20 kHz and filtered at 3-4 kHz using a Multiclamp 700b
623 amplifier (Axon Instruments, Union City, CA), acquired using a version of the MATLAB-based (MathWorks,
624 Natick, MA) acquisition suite, ScanImage (Pologruto et al., 2003).
625
626 **Current clamp recordings**
627 UBCs were targeted using a D1 cre;Tdt transgenic mouse line (P20-40). Slices were perfused with ACSF at
628 RT (22-24 ºC). For current clamp recording any cells with a series resistance >40 MΩ or an action potential
629 peak below 10 mV were excluded from analysis. Intracellular solution used was (in mM) 135 K-gluconate, 4

630 KCl,10 HEPES, 10 Na-phosphocreatine, 4 MgATP, 0.4 Na_2GTP, 1 EGTA, 20 μM Alexa 488 (pH 7.2-7.3,
631 295-298 mOsm/L). Every sweep was 15 seconds long, with a 20 second ITI between each trial. Within each
632 trial, a 500 ms hyperpolarizing step 10-20 pA was injected in order to measure input resistance. In cells that
633 did not have spontaneous firing we injected a 500 ms long depolarizing pulse to assess cell health and ability
634 to fire action potentials. Both the period of hyperpolarizing pulse and the depolarizing pulse were excluded
635 from analysis of spontaneous firing rate. We analyzed spontaneous activity, passive membrane properties,
636 and action potential shape. After break-in we waited ~13 minutes period before acquiring baseline firing
637 properties of the UBCs. The baseline period lasted ~7 min (20 trials) before we applied SKF81297. To
638 activate Drd1 receptors we puff applied SKF81297 (500 μM) using a 300 ms long PicoSpritzer puff (Parker
639 Hannifin, Hollis, NH). The drug was applied once per trial (20 s ITI) for a 10-minute period (30 trials). We
640 continued recording after drug application for a 10-minute (30 trials) washout period. The glass puff pipette
641 was pulled to have a ~5 μm opening. The puff pipette was placed 20-40 μm above tissue surface and 50-75
642 μm away from cell on the x-axis. Care was taken to ensure there was no movement of the slice due to the
643 puff. After the recording, each UBC was imaged to verify that it was filled with Alexa dye, and then a 10X
644 magnification image was taken to record location within the cerebellum.
645
646 **Cell attached recordings**
647 UBCs were targeted using a D1 cre;tdTomato transgenic mouse line (P20-40). Cell-attached recordings were
648 performed in ACSF (32-34ºC). Internal electrode solution contained (in mM): 125 $CsMeSO_3$, 5 HEPES-Cs,
649 0.4 EGTA, 10 Phosphocreatine disodium salt, 2 ATP-Mg, 0.5 GTP-Mg, 5 TEA-Cl, 2 QX314-Cl, 20 μM Alexa
650 488 (pH 7.2-7.3, 295-298 mOsm/L). Every sweep was 15 seconds long, ITI 20 seconds. After a ~16 min (50
651 trials) baseline period we flowed in 10 μM SKF81297 (Tocris 1447) into the bath. Cells showing spontaneous
652 firing were included in analysis for continual monitoring of cell health.
653
654 **Voltage clamp recordings**
655 UBCs were targeted using a D1-cre;tdT transgenic mouse line (P20-40). Voltage clamp recordings were
656 performed in ACSF (32-34ºC). Cells were excluded if they had a series resistance >25 MΩ or if series
657 resistance changed >20% during the recording. We did not use series resistance compensation. The internal
658 electrode solution contained (in mM): 125 $CsMeSO_3$, 5 HEPES-Cs, 0.4 EGTA, 10 Phosphocreatine disodium
659 salt, 2 ATP-Mg, 0.5 GTP-Mg, 5 TEA-Cl, 2 QX314-Cl, 20 μM Alexa 488 (pH 7.2-7.3, 295-298 mOsm/L). In
660 order to isolate NMDAR currents, 1 μM Gabazine (Tocris, 1262), 1 μM NBQX (Tocris, 0373), 1 μM strychnine
661 (Sigma-Aldrich, S8753) were added to the ACSF bath. Cells were held at +40 mV and we used 0 mM MgCl
662 to minimize the Mg block of NMDA receptors. A tungsten bipolar electrode (CBAPB75, FHC Inc) was lowered
663 into nearby white matter at least 100 μm away from UBC being recorded. Each electrical stimulation
664 consisted of 5 pulses, 200 Hz, 100-150 μA, 50-80 μs pulse width. Each trial was 7 seconds long, with an
665 intertrial interval of 30 seconds. Every trial included a 500 ms long 20 mV hyperpolarizing pulse to measure

666 series resistance. We acquired current traces during a baseline period of 20 minutes (40 trials), followed by
667 a flow-in of SKF81297 (10μM) for 15 minutes (30 trials) before washing out the drug.
668
669 *Optogenetic stimulation of Drd1-Cre UBCs*
670 Pkj cells within 100 μm of ChR2-EYFP expressing UBCs were targeted for recording. Recordings were
671 performed in ACSF (32-34 ºC). We recorded baseline firing rate of Purkinje cells in cell-attached mode, loose
672 seal (50-200 M Ohms). To stimulate ChR2 in UBCs we used trains of light pulses (1 ms, 10-20 Hz, 20 pulses,
673 460 nM, 2-5 mW) delivered through a 60X water-immersion objective (Olympus, Tokyo, Japan) with CoolLED
674 PE4000 widefield illumination (CoolLED Ltd., Andover, UK). Every trial was 15 seconds long, with an ITI of
675 20 seconds. After a ~7 min (20 trials) baseline period, we stimulated ChR2 for 30 trials. Afterwards a 10-
676 minute (30 trials) recording with no stimulation was acquired. For each slice, we verified that we could reliably
677 evoke action potentials in nearby EYFP+ UBC with this stimulation protocol.
678
679 For the experiments with EPSC and IPSC recordings, we used an internal solution consisting of 125
680 $CsMeSO_3$, 5 HEPES-Cs, 0.4 EGTA, 10 Phosphocreatine disodium salt, 2 ATP-Mg, 0.5 GTP-Mg, 5 TEA-Cl,
681 2 QX314-Cl, 20 μM Alexa 488 (pH 7.2-7.3, 295-298 mOsm/L). We first achieved a Giga-Ohm seal on the Pkj
682 cell before recording cell-attached action potentials, to evaluate the response of Pkjs to UBC optogenetic
683 activation before breaking into the Pkj cell and recording synaptic currents. We recorded EPSCs while
684 holding the cell at -70 mV (5 trials), then slowly increasing the holding voltage to 0 mV and recording IPSCs
685 (5 trials).
686
687 *IPSC recordings in UBCs*
688 Drd1-Cre animals were injected with AAV1-PCP2-ChR2-mCherry and AAV8-Flex-GFP. Acutely prepared
689 brain slices were perfused with ACSF at RT (22-24ºC) to slow down spontaneous firing rate of Pkj cells. We
690 used epifluorescence to verify expression of mCherry in nearby Pkj cells, with very brief GFP illumination to
691 target UBCs for patch clamping without stimulating ChR2. We used an internal solution with a high
692 concentration of Cl^- ions (in mM): 150 CsCl, 4 NaCl, 0.5 $CaCl_2$, 10 HEPES-Cs, 5 EGTA-Cs, 10
693 Phosphocreatine disodium salt, 2 ATP-Mg, 0.5 GTP-Na, 2 QX314-Br, 20 μM Alexa 488 (pH 7.2-7.3, 295-298
694 mOsm/L). Starting 5 minutes after break-in, we recorded 10 trials/UBC, where every trial was 15 seconds
695 long, with an ITI of 60 seconds. During every trial, we delivered an optogenetic stimulus train (1 ms, 100 Hz,
696 100 pulses, 460 nM, 2-5 mW) through a 60X water-immersion objective (Olympus, Tokyo, Japan) with
697 CoolLED illumination PE4000. For a subset of experiments, after 5 trials we added 10 μM Gabazine to the
698 bath. For every slice, cell-attached recordings were used to verify efficient optogenetic stimulation of Pkj cell
699 firing.
700
701 **Two-photon imaging and glutamate uncaging experiments**

Slices were perfused with ACSF at RT (22-24ºC). Experiments were done on a modified acute slice electrophysiology Scientifica microscope using a 60X water immersion objective**.** Two mode-locked Ti:Sapphire lasers (Mai Tai eHP and Mai Tai eHP DS, Newport) were used for two-photon fluorescence imaging and for uncaging, with the wavelengths of 910 nm and 725 nm, respectively (Banala et al., 2018; Chen et al., 2020; Kozorovitskiy et al., 2015; Wu et al., 2021; Xiao et al., 2018). The location of the laser beam was controlled by a two-dimensional galvanometer scanning mirror system (HSA Galvo 8315K, Cambridge Technology). Fluorescence emission was passed through a dichroic beamsplitter (FF670-SDi01-26x38, Semrock) and a bandpass filter (FF02-520/28, Semrock). Emission light was collected by two PMTs (H10770P, Hamamatsu). MATLAB script-based data acquisition software ScanImage (Pologruto et al., 2003) was used to acquire images. Laser intensity was controlled by Pockels cells, with laser power at the sample plane of 10-15 mW. For glutamate uncaging experiments, to isolate NMDAR currents the following drugs were included in the ACSF bath: 1 μM TTX (Tocris, 1069), 1 μM Gabazine (Tocris, 1262), 1 μM NBQX (Tocris, 0373), 1 μM strychnine (Sigma-Aldrich, S8753), 1 μM Pyr-3 (Tocris,3753), 1 mM MNI-caged-L-glutamate. Images were acquired at 2X magnification, sampled at 15.6 Hz continuously, 1 ms dwell time per pixel, 256 x 256. Uncaging was performed using 1 ms pulses at 725 nm power (10-20 mW). Each trial was 15 seconds long with a 60 second ITI between trials. The mean NMDAR current for each cell was calculated across all trials that evoked a response.

For two-photon experiments imaging $GRAB_{DA2h}$ data were acquired with a 3.9 Hz sampling rate, each trial lasted ~25 seconds with an ITI of 150 seconds. A monopolar stimulating electrode was placed 100-200 μm away from cell being imaged within white matter tracts. The electrical stimulation (50 pulses, 50 Hz, 100 μs pulse width, 100-300 μA) was delivered every 150 seconds. Five to ten baseline trials were acquired before the flow-in of Drd2 antagonist (1 μM L-741,626). For optogenetic experiments, the same imaging parameters as for electrical stimulation experiments were used. Instead of electrical stimulation, CoolLED pe300 (CoolLED Ltd., Andover, UK) was used to activate ChR2 (20 pulses at 39 Hz, 2 ms pulses, 460 nm, 3-5 mW/cm^2). For these experiments we visually verified the expression of ChR2+ in LC axons post hoc, using the fused mCherry fluorophore. To avoid activating TH+ Pkj cells, we excluded acute slices from animals with Pkj cells expressing mCherry.

Pharmacology

All drugs were purchased from Sigma Aldrich (St. Louis, MO), or Tocris (Bristol, UK). SKF 81297 hydrobromide (Tocris, 1447) was applied either as puff (500 μM) or flow in (10 μM) depending on experiment type. All other drugs were bath applied: SCH-39166 hydrobromide (Tocris,2299), SCH-23390 hydrochloride (Tocris, 0925), SKF-83566 hydrobromide (Tocris, 1586), Strychnine (Sigma-Aldrich, 8753), Tetraethylammonium chloride (Sigma-Aldrich, 86614), TTX (Tocris Bioscience, 1069), (RS)-CPP (Tocris Bioscience, 0173), NBQX (Tocris Bioscience, 0373), SR 95531 hydrobromide (Tocris Bioscience, 1262), MNI-caged-L-glutamate (Tocris Biosciences 1490), L-741,626 (Tocris Bioscience, 1003), Pyr-3 (Tocris,3753).

739

740 **Analysis and statistics**

741 No statistical methods were used to pre-determine sample sizes, but our sample sizes are similar to those
742 reported in previous publications using similar methods. Custom MATLAB (MathWorks, Natick, MA) scripts
743 were used for analysis of electrophysiology data. For current clamp recordings we analyzed membrane
744 voltage, firing rate, input resistance, and action potential half width. Membrane voltage was calculated using
745 a median filter to exclude changes due to action potential firing. Data from cell-attached recordings were
746 used to quantify spontaneous firing rate without perturbing the membrane. Data from voltage clamp
747 recordings were analyzed for width and peak of evoked current traces. Fluorescence intensity signals from
748 $GRAAB_{DA2h}$ imaging experiments were measured in FIJI (Schindelin et al., 2012), data were then analyzed
749 in MATLAB. Fluorescence signal for each trial was normalized as ΔF/F. Summary values were aggregated
750 in GraphPad Prism 5 (GraphPad, LaJolla, CA) for all statistical tests. All population data were tested for
751 normality using Shapiro-Wilk normality test, D'Agostino & Pearson omnibus normality test, and KS normality
752 test. Paired t-test or paired Mann-Whitney U test were used, as appropriate. For comparisons between
753 current clamp datasets, we used Kruskal-Wallis test with Dunn's multiple comparison post hoc test. In all
754 figures, bars represent mean +/- SEM. Group allocation was randomized, as indicated in our methods section
755 under the analysis and statistics subsection. All data analysis used batch processing with the same code
756 and parameters. For histological analyses comparing expression of proteins or mRNA between brain regions
757 the same intensity and size thresholds were applied.

758

759 **REFERENCES**

760 Abbott, L.C., Isaacs, K.R., and Heckroth, J.A. (1996). Co-localization of tyrosine hydroxylase and Zebrin II
761 immunoreactivities in Purkinje cells of the mutant mice, tottering and tottering/leaner. Neuroscience *71*,
762 461–475.

763 Altman, J., and Bayer, S.A. (1977). Time of origin and distribution of a new cell type in the rat cerebellar
764 cortex. Exp. Brain Res. *29*, 265–274.

765 Aosaki, T., Kiuchi, K., and Kawaguchi, Y. (1998). Dopamine D1-like receptor activation excites rat striatal
766 large aspiny neurons in vitro. J. Neurosci. *18*, 5180–5190.

767 Asmus, S.E., Anderson, E.K., Ball, M.W., Barnes, B.A., Bohnen, A.M., Brown, A.M., Hartley, L.J., Lally,
768 M.C., Lundblad, T.M., Martin, J.B., et al. (2008). Neurochemical characterization of tyrosine hydroxylase-
769 immunoreactive interneurons in the developing rat cerebral cortex. Brain Res. *1222*, 95–105.

770 Austin, M.C., Schultzberg, M., Abbott, L.C., Montpied, P., Evers, J.R., Paul, S.M., and Crawley, J.N.
771 (1992). Expression of tyrosine hydroxylase in cerebellar Purkinje neurons of the mutant tottering and leaner
772 mouse. Mol. Brain Res. *15*, 227–240.

773 Bäckman, C., Malik, N., Zhang, Y., Shan, L., Grinberg, A., Hoffer, B., Westphal, H., and Tomac, A. (2006).
774 Characterization of a mouse strain expressing Cre recombinase from the 3' untranslated region of the
775 dopamine transporter locus. Genesis *44*, 383–390.

776 Balmer, T.S., and Trussell, L.O. (2019). Selective targeting of unipolar brush cell subtypes by cerebellar
777 mossy fibers. Elife *8*, 1–28.

778 Banala, S., Arvin, M.C., Bannon, N.M., Jin, X.T., Macklin, J.J., Wang, Y., Peng, C., Zhao, G., Marshall, J.J.,
779 Gee, K.R., et al. (2018). Photoactivatable drugs for nicotinic optopharmacology. Nat. Methods *15*, 347–
780 350.

781 Basile, A.S., and Dunwiddie, T. V. (1984). Norepinephrine elicits both excitatory and responses from
782 Purkinje cells in the in vitro rat cerebellar slice. Brain Res. *296*, 15–25.

783 Beas, B.S., Wright, B.J., Skirzewski, M., Leng, Y., Hyun, J.H., Koita, O., Ringelberg, N., Kwon, H.-B.,
784 Buonanno, A., and Penzo, M.A. (2018). The locus coeruleus drives disinhibition in the midline thalamus via
785 a dopaminergic mechanism. Nat. Neurosci. *21*, 963–973.

786 Bloom, F.E., Hoffer, B.J., and Siggins, G.R. (1971). Studies on norepinephrine-containing afferents to
787 Purkinje cells of rat cerebellum. I. Localization of the fibers and their synapses. Brain Res. *25*, 501–521.

788 Bolte, S., and Cordelieres, F.P. (2006). A guided tour into subcellular colocalisation analysis in light
789 microscopy. J. Microsc. *224*, 13–232.

790 Carey, M.R., and Regehr, W.G. (2009). Noradrenergic Control of Associative Synaptic Plasticity by
791 Selective Modulation of Instructive Signals. Neuron *62*, 112–122.

792 Cerminara, N.L., Lang, E.J., Sillitoe, R. V., and Apps, R. (2015). Redefining the cerebellar cortex as an
793 assembly of non-uniform Purkinje cell microcircuits. Nat. Rev. Neurosci. *16*, 79–93.

794 Chand, A.N., Galliano, E., Chesters, R.A., and Grubb, M.S. (2015). A distinct subtype of dopaminergic
795 interneuron displays inverted structural plasticity at the axon initial segment. J. Neurosci. *35*, 1573–1590.

796 Chen, C., Soto, G., Dumrongprechachan, V., Bannon, N., Kang, S., Kozorovitskiy, Y., and Parisiadou, L.
797 (2020). Pathway-specific dysregulation of striatal excitatory synapses by LRRK2 mutations. Elife *9*, 1–26.

798 Chen, G., Greengard, P., and Yan, Z. (2004). Potentiation of NMDA receptor currents by dopamine D1
799 receptors in prefrontal cortex. Proc. Natl. Acad. Sci. U. S. A. *101*, 2596–2600.

800 Chen, L., Bohanick, J.D., Nishihara, M., Seamans, J.K., and Yang, C.R. (2007). Dopamine D1/5 receptor-
801 mediated long-term potentiation of intrinsic excitability in rat prefrontal cortical neurons: Ca2+-dependent
802 intracellular signaling. J. Neurophysiol. *97*, 2448–2464.

803 Chuhma, N., Mingote, S., Yetnikoff, L., Kalmbach, A., Ma, T., Ztaou, S., Sienna, A.-C., Tepler, S., Poulin,
804 J.-F., Ansorge, M., et al. (2018). Dopamine neuron glutamate cotransmission evokes a delayed excitation
805 in lateral dorsal striatal cholinergic interneurons. Elife *7*, 1–29.

806 Chung, S.-H., Marzban, H., Watanabe, M., and Hawkes, R. (2009). Phospholipase Cbeta4 expression
807 identifies a novel subset of unipolar brush cells in the adult mouse cerebellum. Cerebellum *8*, 267–276.

808 Chung, S.-H., Kim, C.-T., Jeong, Y.-G., and Lee, N.-S. (2010). TBR2-immunopsitive unipolar brush cells
809 are associated with ectopic zebrin II-immunoreactive Purkinje cell clusters in the cerebellum of scrambler
810 mice. Anat. Cell Biol. *43*, 72.

811 Diana, M.A., Otsu, Y., Maton, G., Collin, T., Chat, M., and Dieudonne, S. (2007). T-Type and L-Type Ca2+
812 Conductances Define and Encode the Bimodal Firing Pattern of Vestibulocerebellar Unipolar Brush Cells.
813 J. Neurosci. *27*, 3823–3838.

814 Dizon, M.J., and Khodakhah, K. (2011). The role of interneurons in shaping Purkinje cell responses in the
815 cerebellar cortex. J. Neurosci. *31*, 10463–10473.

816 El-Shamayleh, Y., Kojima, Y., Soetedjo, R., and Horwitz, G.D. (2017). Selective Optogenetic Control of
817 Purkinje Cells in Monkey Cerebellum. Neuron 1–12.

818 Englund, C. (2006). Unipolar Brush Cells of the Cerebellum Are Produced in the Rhombic Lip and Migrate
819 through Developing White Matter. J. Neurosci. *26*, 9184–9195.

820 Giovannucci, A., Badura, A., Deverett, B., Najafi, F., Pereira, T.D., Gao, Z., Ozden, I., Kloth, A.D.,
821 Pnevmatikakis, E., Paninski, L., et al. (2017). Cerebellar granule cells acquire a widespread predictive
822 feedback signal during motor learning. Nat. Neurosci. *20*, 727–734.

823 Gong S. Zheng C., D.M.L. et al (2003). A gene expression atlas of the central nervous system based on
824 artificial chromosomes. Nature *425*, 917–925.

825 Guo, C., Witter, L., Rudolph, S., Elliott, H.L., Ennis, K.A., and Regehr, W.G. (2016). Purkinje Cells Directly
826 Inhibit Granule Cells in Specialized Regions of the Cerebellar Cortex. Neuron *91*, 1330–1341.

827 Harada, K., Ito, M., Wang, X., Tanaka, M., Wongso, D., Konno, A., Hirai, H., Hirase, H., Tsuboi, T., and
828 Kitaguchi, T. (2017). Red fluorescent protein-based cAMP indicator applicable to optogenetics and in vivo
829 imaging. Sci. Rep. *7*, 1–9.

830 Hernandez-Lopez, S., Bargas, J., Surmeier, D.J., Reyes, A., and Galarraga, E. (1997). D1 receptor
831 activation enhances evoked discharge in neostriatal medium spiny neurons by modulating an L-type Ca2+
832 conductance. J Neurosci *17*, 3334–3342.

833 Huang, S., and Uusisaari, M.Y. (2013). Physiological temperature during brain slicing enhances the quality

834 of acute slice preparations. Front. Cell. Neurosci. *7*.

835 Huang, Y., Zhang, Q., Song, N.-N., Zhang, L., Sun, Y.-L., Hu, L., Chen, J.-Y., Zhu, W., Li, J., and Ding, Y.-
836 Q. (2016). Lrp5/6 are required for cerebellar development and for suppressing TH expression in Purkinje
837 cells via β-catenin. Mol. Brain *9*, 7.

838 Hurley, M.J., Mash, D.C., and Jenner, P. (2003). Markers for dopaminergic neurotransmission in the
839 cerebellum in normal individuals and patients with Parkinson's disease examined by RT-PCR. Eur. J.
840 Neurosci. *18*, 2668–2672.

841 Kalmbach, B.E., Davis, T., Ohyama, T., Riusech, F., Nores, W.L., and Mauk, M.D. (2010). Cerebellar
842 cortex contributions to the expression and timing of conditioned eyelid responses. J. Neurophysiol. *103*,
843 2039–2049.

844 Kawahara, H., Kawahara, Y., and Westerink, B.H.C. (2001). The noradrenaline-dopamine interaction in the
845 rat medial prefrontal cortex studied by multi-probe microdialysis. Eur. J. Pharmacol. *418*, 177–186.

846 Kempadoo, K.A., Mosharov, E. V., Choi, S.J., Sulzer, D., and Kandel, E.R. (2016). Dopamine release from
847 the locus coeruleus to the dorsal hippocampus promotes spatial learning and memory. Proc. Natl. Acad.
848 Sci. *113*, 14835–14840.

849 Kim, J.A., Sekerková, G., Mugnaini, E., and Martina, M. (2012). Electrophysiological, morphological, and
850 topological properties of two histochemically distinct subpopulations of cerebellar unipolar brush cells.
851 Cerebellum *11*, 1012–1021.

852 Kim, Y.S., Shin, J.H., Hall, F.S., and Linden, D.J. (2009). Dopamine signaling is required for depolarization-
853 induced slow current in cerebellar Purkinje cells. J. Neurosci. *29*, 8530–8538.

854 Kozorovitskiy, Y., Peixoto, R., Wang, W., Saunders, A., and Sabatini, B.L. (2015). Neuromodulation of
855 excitatory synaptogenesis in striatal development. Elife *4*, e10111.

856 Lahiri, A.K., and Bevan, M.D. (2020). Dopaminergic Transmission Rapidly and Persistently Enhances
857 Excitability of D1 Receptor-Expressing Striatal Projection Neurons. Neuron *106*, 277-290.e6.

858 Lanore, F., Rothman, J.S., Coyle, D., and Silver, R.A. (2019). Norepinephrine controls the gain of the
859 inhibitory circuit in the cerebellar input layer. BioRxiv 567172.

860 Lee, N.S., Kim, C.T., Han, S.Y., Kawk, J.H., Sawada, K., Fukui, Y., and Jeong, Y.G. (2006). The absence
861 of phosphorylated tyrosine hydroxylase expression in the Purkinje cells of the ataxic mutant pogo mouse.
862 J. Vet. Med. Ser. C Anat. Histol. Embryol. *35*, 178–183.

863 Li, B., Zhu, J., and Wang, J. (2014). Histaminergic afferent system in the cerebellum : structure and
864 function. Cerebellum & Ataxias *1*, 1–9.

865 Lippiello, P., Hoxha, E., Volpicelli, F., Lo Duca, G., Tempia, F., and Miniaci, M.C. (2015). Noradrenergic
866 modulation of the parallel fiber-Purkinje cell synapse in mouse cerebellum. Neuropharmacology *89*, 33–42.

867 Locke, T.M., Soden, M.E., Miller, S.M., Hunker, A., Knakal, C., Licholai, J.A., Dhillon, K.S., Keene, C.D.,
868 Zweifel, L.S., and Carlson, E.S. (2018). Dopamine D1 Receptor–Positive Neurons in the Lateral Nucleus of
869 the Cerebellum Contribute to Cognitive Behavior. Biol. Psychiatry *84*, 401–412.

870 Locke, T.M., Fujita, H., Hunker, A., Johanson, S.S., Darvas, M., du Lac, S., Zweifel, L.S., and Carlson, E.S.
871 (2020). Purkinje Cell-Specific Knockout of Tyrosine Hydroxylase Impairs Cognitive Behaviors. Front. Cell.
872 Neurosci. *14*, 1–16.

873 Madisen, L., Zwingman, T.A., Sunkin, S.M., Oh, S.W., Zariwala, H.A., Gu, H., Ng, L.L., Palmiter, R.D.,
874 Hawrylycz, M.J., Jones, A.R., et al. (2010). A robust and high-throughput Cre reporting and
875 characterization system for the whole mouse brain. Nat. Neurosci. *13*, 133–140.

876 Mansour, A., Meador-Woodruff, J.H., Zhou, Q.Y., Civelli, O., Akil, H., and Watson, S.J. (1991). A
877 comparison of D1 receptor binding and mRNA in rat brain using receptor autoradiographic and in situ
878 hybridization techniques. Neuroscience *45*, 359–371.

879 Melchitzky, D. (2000). Tyrosine Hydroxylase- and Dopamine Transporter-Immunoreactive Axons in the
880 Primate Cerebellum Evidence for a Lobular- and Laminar-Specific Dopamine Innervation.
881 Neuropsychopharmacology *22*, 466–472.

882 Mugnaini, E., and Floris, A. (1994). The unipolar brush cell: A neglected neuron of the mammalian
883 cerebellar cortex. J. Comp. Neurol. *339*, 174–180.

884 Nelson, T.E., King, J.S., and Bishop, G.A. (1997). Distribution of tyrosine hydroxylase-immunoreactive
885 afferents to the cerebellum differs between species. J. Comp. Neurol. *379*, 443–454.

886 Ollion, J., Cochennec, J., Loll, F., Escudé, C., and Boudier, T. (2013). TANGO: A generic tool for high-
887 throughput 3D image analysis for studying nuclear organization. Bioinformatics *29*, 1840–1841.

888 Panagopoulos, N.T., Papadopoulos, G.C., and Matsokis, N. a. (1991). Dopaminergic innervation and
889 binding in the rat cerebellum. Neurosci. Lett. *130*, 208–212.

890 Panagopoulos, N.T., Matsokis, N. a, and Valcana, T. (1993). Cerebellar and striatal dopamine receptors:
891 effects of reeler and weaver murine mutations. J. Neurosci. Res. *35*, 499–506.

892 Patriarchi, T., Cho, J.R., Merten, K., Howe, M.W., Marley, A., Xiong, W., Folk, R.W., Broussard, G.J.,
893 Liang, R., Jang, M.J., et al. (2018). Ultrafast neuronal imaging of dopamine dynamics with designed
894 genetically encoded sensors. *4422*, 1–15.

895 Pologruto, T.A., Sabatini, B.L., and Svoboda, K. (2003). ScanImage: Flexible software for operating laser

896 scanning microscopes. Biomed. Eng. Online *2*, 1–9.

897 Poulin, J.F., Caronia, G., Hofer, C., Cui, Q., Helm, B., Ramakrishnan, C., Chan, C.S., Dombeck, D.A.,
898 Deisseroth, K., and Awatramani, R. (2018). Mapping projections of molecularly defined dopamine neuron
899 subtypes using intersectional genetic approaches. Nat. Neurosci. *21*, 1260–1271.

900 Rajakumar, N., Hrycyshyn, A.W., and Flumerfelt, B.A. (1992). Afferent organization of the lateral reticular
901 nucleus in the rat: An anterograde tracing study. Anat. Embryol. (Berl). *185*, 25–37.

902 Raymond, J.L., and Lisberger, S.G. (1998). Neural Learning Rules for the Vestibulo-Ocular Reflex. *18*,
903 9112–9129.

904 Reardon, T.R., Murray, A.J., Turi, G.F., Wirblich, C., Croce, K.R., Schnell, M.J., Jessell, T.M., and
905 Losonczy, A. (2016). Rabies Virus CVS-N2cδG Strain Enhances Retrograde Synaptic Transfer and
906 Neuronal Viability. Neuron *89*, 711–724.

907 Requarth, T., and Sawtell, N.B. (2014). Plastic Corollary Discharge Predicts Sensory Consequences of
908 Movements in a Cerebellum-Like Circuit. Neuron *82*, 896–907.

909 Sabatini, B.L., and Tian, L. (2020). Imaging Neurotransmitter and Neuromodulator Dynamics In Vivo with
910 Genetically Encoded Indicators. Neuron *108*, 17–32.

911 Sakai, M., Fujii, T., Karasawa, N., Arai, R., and Nagatsu, I. (1995). Enhanced expression of tyrosine
912 hydroxylase and aromatic l-amino acid decarboxylase in cerebellar Purkinje cells of mouse after
913 hyperosmotic stimuli. Neurosci. Lett. *194*, 142–144.

914 Sawada, K., Ando, M., Sakata-Haga, H., Sun, X., Jeong, Y., Hisano, S., Takeda, N., and Fukui, Y. (2004).
915 Abnormal expression of tyrosine hydroxylase not accompanied by phosphorylation at serine 40 in
916 cerebellar Purkinje cells of ataxic mutant mice, rolling mouse Nagoya and dilute-lethal. Congenit. Anom.
917 (Kyoto). *44*, 46–50.

918 Schindelin, J., Arganda-Carreras, I., Frise, E., Kaynig, V., Longair, M., Pietzsch, T., Preibisch, S., Rueden,
919 C., Saalfeld, S., Schmid, B., et al. (2012). Fiji: An open-source platform for biological-image analysis. Nat.
920 Methods *9*, 676–682.

921 Schneider, C.A., Rasband, W.S., and Eliceiri, K.W. (2012). NIH Image to ImageJ: 25 years of image
922 analysis. Nat. Methods *9*, 671–675.

923 Schwarz, L.A., Miyamichi, K., Gao, X.J., Beier, K.T., Weissbourd, B., DeLoach, K.E., Ren, J., Ibanes, S.,
924 Malenka, R.C., Kremer, E.J., et al. (2015). Viral-genetic tracing of the input–output organization of a central
925 noradrenaline circuit. Nature *524*, 88–92.

926 Schweighofer, N., Doya, K., and Kuroda, S. (2004). Cerebellar aminergic neuromodulation: towards a

927 functional understanding. Brain Res. Brain Res. Rev. *44*, 103–116.

928 Sekerková, G., Kim, J.-A., Nigro, M.J., Becker, E.B.E., Hartmann, J., Birnbaumer, L., Mugnaini, E., and
929 Martina, M. (2013). Early onset of ataxia in moonwalker mice is accompanied by complete ablation of type
930 II unipolar brush cells and Purkinje cell dysfunction. J. Neurosci. *33*, 19689–19694.

931 Singla, S., Dempsey, C., Warren, R., Enikolopov, A.G., and Sawtell, N.B. (2017). A cerebellum-like circuit
932 in the auditory system cancels responses to self-generated sounds. Nat. Neurosci. *20*, 943–950.

933 Skeberdis, V.A., Chevaleyre, V., Lau, C.G., Goldberg, J.H., Pettit, D.L., Suadicani, S.O., Lin, Y., Bennett,
934 M.V.L., Yuste, R., Castillo, P.E., et al. (2006). Protein kinase A regulates calcium permeability of NMDA
935 receptors. Nat. Neurosci. *9*, 501–510.

936 Stoof, J.C., and Kebabian, J.W. (1984). Two dopamine receptors: Biochemistry, physiology and
937 pharmacology. Life Sci. *35*, 2281–2296.

938 Sun, F., Zeng, J., Jing, M., Zhou, J., Feng, J., Owen, S.F., Luo, Y., Li, F., Wang, H., Yamaguchi, T., et al.
939 (2018). A Genetically Encoded Fluorescent Sensor Enables Rapid and Specific Detection of Dopamine in
940 Flies, Fish, and Mice. Cell *174*, 481-496.e19.

941 Sun, F., Zhou, J., Dai, B., Qian, T., Zeng, J., Li, X., Zhuo, Y., Zhang, Y., Wang, Y., Qian, C., et al. (2020).
942 Next-generation GRAB sensors for monitoring dopaminergic activity in vivo. Nat. Methods *17*, 1156–1166.

943 Surmeier, D.J., and Kitai, S.T. (1993). D1 and D2 dopamine receptor modulation of sodium and potassium
944 currents in rat neostriatal neurons. Prog. Brain Res. *99*, 309–324.

945 Surmeier, D.J., Bargas, J., Hemmings, H.C., Nairn, A.C., and Greengard, P. (1995). Modulation of calcium
946 currents by a D1 dopaminergic protein kinase/phosphatase cascade in rat neostriatal neurons. Neuron *14*,
947 385–397.

948 Takada, M., Sugimoto, T., and Hattori, T. (1993). Tyrosine hydroxylase immunoreactivity in cerebellar
949 Purkinje cells of the rat. Neurosci. Lett. *150*, 61–64.

950 Takeuchi, T., Duszkiewicz, A.J., Sonneborn, A., Spooner, P.A., Yamasaki, M., Watanabe, M., Smith, C.C.,
951 Fernández, G., Deisseroth, K., Greene, R.W., et al. (2016). Locus coeruleus and dopaminergic
952 consolidation of everyday memory. Nature *537*, 357–362.

953 Wagner, M.J., Kim, T.H., Savall, J., Schnitzer, M.J., and Luo, L. (2017). Cerebellar granule cells encode
954 the expectation of reward. Nature *544*, 96–100.

955 Warren, R., and Sawtell, N.B. (2016). A comparative approach to cerebellar function: insights from
956 electrosensory systems. Curr. Opin. Neurobiol. *41*, 31–37.

957 Watanabe, D., and Nakanishi, S. (2003). mGluR2 postsynaptically senses granule cell inputs at golgi cell
958 synapses. Neuron *39*, 821–829.

959 Weihe, E., Depboylu, C., Schütz, B., Schäfer, M.K.H., and Eiden, L.E. (2006). Three types of tyrosine
960 hydroxylase-positive CNS neurons distinguished by dopa decarboxylase and VMAT2 co-expression. Cell.
961 Mol. Neurobiol. *26*, 659–678.

962 Woodruff-pak, D.S. (1993). Eyeblink Classical Conditioning in H . M .: Delay and Trace Paradigms. Behav.
963 Neurosci. *107*, 911–925.

964 Wu, H.S., Sugihara, I., and Shinoda, Y. (1999). Projection patterns of single mossy fibers originating from
965 the lateral reticular nucleus in the rat cerebellar cortex and nuclei. J. Comp. Neurol. *411*, 97–118.

966 Wu, M., Minkowicz, S., Dumrongprechachan, V., Hamilton, P., and Kozorovitskiy, Y. (2021). Ketamine
967 rapidly enhances glutamate-evoked dendritic spinogenesis in medial prefrontal cortex through
968 dopaminergic mechanisms. Biol. Psychiatry.

969 Xenias, H.S., Ibanez-Sandoval, O., Koos, T., and Tepper, J.M. (2015). Are Striatal Tyrosine Hydroxylase
970 Interneurons Dopaminergic? J. Neurosci. *35*, 6584–6599.

971 Xiao, L., Priest, M.F., and Kozorovitskiy, Y. (2018). Oxytocin functions as a spatiotemporal filter for
972 excitatory synaptic inputs to VTA dopamine neurons. Elife *7*, 1–26.

973 Zampini, V., Liu, J.K., Diana, M.A., Maldonado, P.P., Brunel, N., and Dieudonné, S. (2016). Mechanisms
974 and functional roles of glutamatergic synapse diversity in a cerebellar circuit. Elife *5*, 1–25.

975

976

SUPPLEMENTARY FIGURES

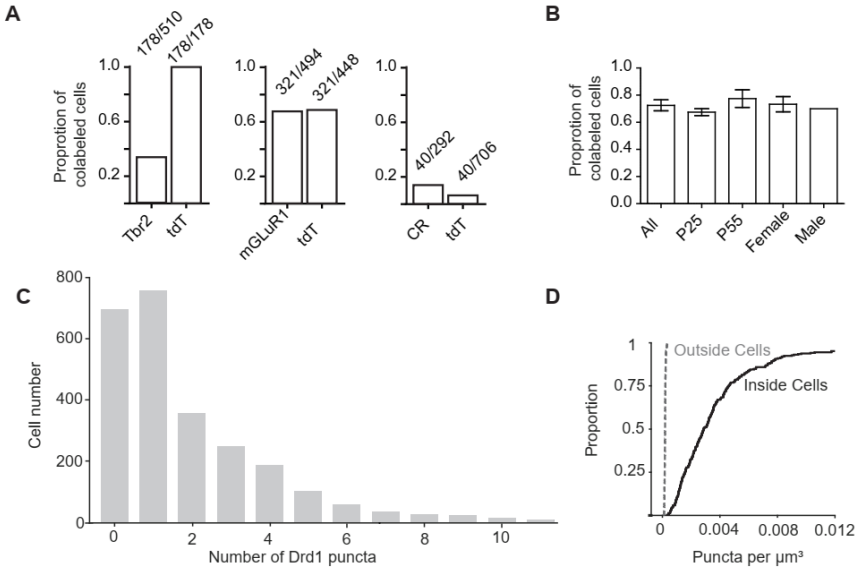

Supplementary Figure 1. Co-localization of tdT+ UBCs with known UBC subtype markers and Drd1 mRNA.

A. The proportion of cells co-labeled by immunohistochemical markers of UBC subtypes and tdT in a Drd1-Cre; tdT mouse line. *Left*: Only a subset of Tbr2+ UBCs were co-labeled by tdTomato, while all tdT+ cells expressed Tbr2 protein. *Center*: tdT+ and mGluR1+ UBCs show substantial overlap. *Right:* Few CR+ UBCs express tdT. Ratios represent the population of co-labeled cells divided by the total number of cells expressing given protein.

B. A comparison of *Drd1*+ cells between two age groups and the sex of the mouse show similar proportion of UBCs that express *Drd1* transcripts. (n=4 total mice, P25 n=2, P55 n=2, Female n=3, Male n=1).

C. A histogram of the number of *Drd1* puncta per each UBC tdT+ soma (n=4 mice, 2553 cells).

D. 3D quantification of *Drd1* puncta per unit volume shows a 40-fold enrichment within the somata of UBCs expressing tdT, compared to regions outside dT+ ROIs.

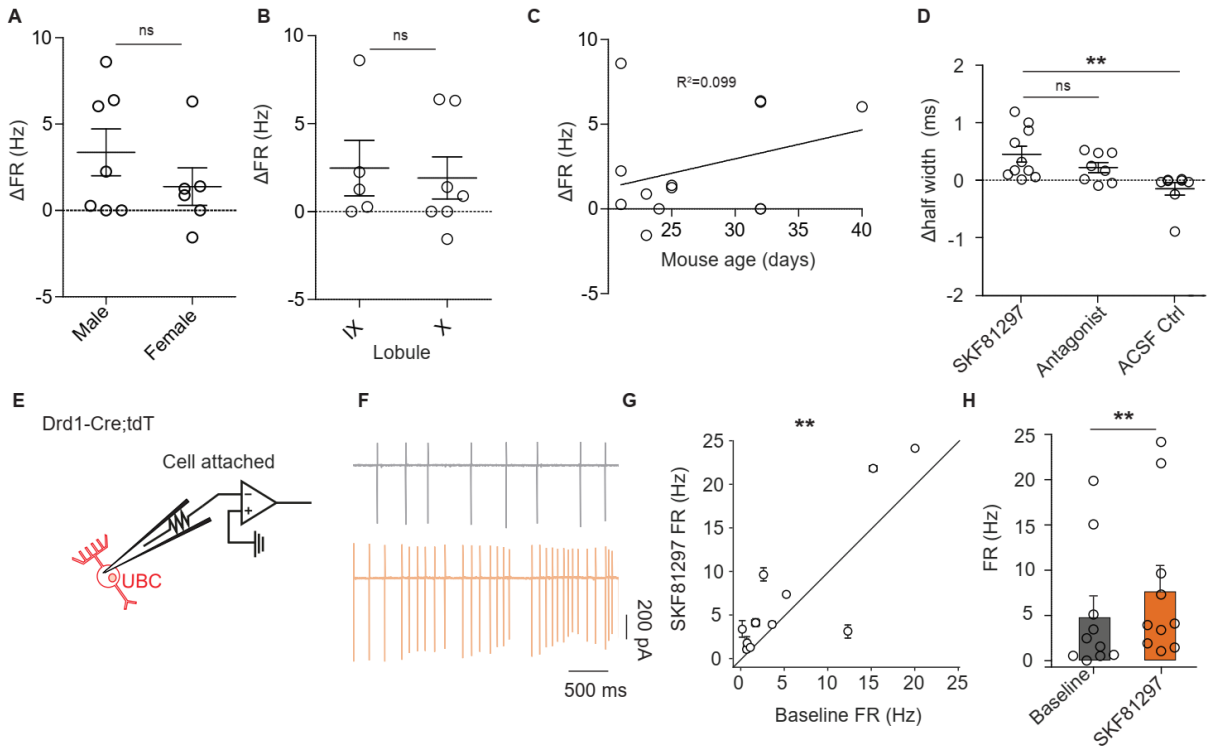

Supplementary Figure 2. Drd1 receptor mediated firing rate changes across age, sex, and recording type.

A. Comparison of changes in firing rate in response to SKF81297 application shows no difference across sex (unpaired t-test, Mann-Whitney U test, p=0.42).

B. Comparison of changes in firing rate in response to SKF81297 application across lobules IX and X of the vermis (unpaired t-test, Mann-Whitney U test, p=0.62).

C. Comparison of changes in firing rate in response to SKF81297 application across age (P20-P40) (R^2=0.099, ns).

D. Comparison of changes in action potential half-width shows an increase with application of SKF81297, but not ACSF (Kruskal-Wallis test, p=0.0026, Dunn's multiple comparison test, *p<0.05, ** p<0.01).

E. Diagram of experimental setup. TdT+ UBCs were targeted with a loose seal patch for cell-attached recording of spontaneous firing.

F. An example trace of a cell-attached recording from a UBC, in the baseline condition and after 10 μM SKF81297 flow in.

G, H. Summary data from cell attached recordings comparing firing rate during the baseline period and after application of SKF81297 (n=9 cells, paired t-test, p= 0.002, *p<0.05, ** p<0.01).